

## Research Article

# Fast and Efficient Numerical Finite Difference Method for Multiphase Image Segmentation

Yibao Li,<sup>1</sup> Sungha Yoon,<sup>2</sup> Jian Wang,<sup>3</sup> Jintae Park,<sup>2</sup> Sangkwon Kim,<sup>2</sup> Chaeyoung Lee,<sup>2</sup> Hyundong Kim,<sup>2</sup> and Junseok Kim <sup>2</sup>

<sup>1</sup>School of Mathematics and Statistics, Xi'an Jiaotong University, Xi'an 710049, China

<sup>2</sup>Department of Mathematics, Korea University, Seoul 02841, Republic of Korea

<sup>3</sup>School of Mathematics and Statistics, Nanjing University of Information Science and Technology, Nanjing 210044, China

Correspondence should be addressed to Junseok Kim; cfdkim@korea.ac.kr

Received 23 July 2021; Revised 13 October 2021; Accepted 5 November 2021; Published 20 November 2021

Academic Editor: Akemi Gálvez

Copyright © 2021 Yibao Li et al. This is an open access article distributed under the Creative Commons Attribution License, which permits unrestricted use, distribution, and reproduction in any medium, provided the original work is properly cited.

We present a simple numerical solution algorithm for a gradient flow for the Modica–Mortola functional and numerically investigate its dynamics. The proposed numerical algorithm involves both the operator splitting and the explicit Euler methods. A time step formula is derived from the stability analysis, and the goodness of fit of transition width is tested. We perform various numerical experiments to investigate the property of the gradient flow equation, to verify the characteristics of our method in the image segmentation application, and to analyze the effect of parameters. In particular, we propose an initialization process based on target objects. Furthermore, we conduct comparison tests in order to check the performance of our proposed method.

## 1. Introduction

We consider a practical and efficient numerical method to solve the following equation:

$$\frac{\partial \phi(\mathbf{x}, t)}{\partial t} = 2\varepsilon \Delta \phi(\mathbf{x}, t) - \frac{\pi}{\varepsilon} \sin(2\pi\phi(\mathbf{x}, t)), \quad \mathbf{x} \in \Omega, t > 0, \quad (1)$$

where  $\phi(\mathbf{x}, t)$  is a phase-field function in space  $\mathbf{x}$  and time  $t$  and  $\varepsilon$  is a positive constant. Here,  $\Omega$  is a bounded domain in  $\mathbb{R}^d$  ( $d = 1, 2$ ). We apply the homogeneous Neumann boundary condition  $\mathbf{n} \cdot \nabla \phi = 0$  on  $\partial\Omega$ , where  $\mathbf{n}$  denotes the unit normal vector to  $\partial\Omega$ . Equation (1) depicts a gradient flow equation in the  $L^2(\Omega)$ -norm for the Modica–Mortola functional [1, 2]:

$$\mathcal{E}(\phi) := \int_{\Omega} \left[ \varepsilon |\nabla \phi|^2 + \frac{1}{\varepsilon} \sin^2(\pi\phi) \right] dx. \quad (2)$$

Figure 1 shows the multiple periodic well potential,  $(1/\varepsilon)\sin^2(\pi\phi)$ , given by the second term in equation (2).

Phase-field models have been actively studied until recently in various fields [3, 4]. Bogosel et al. [5] proposed an efficient phase-field method based on a multiphase  $\Gamma$ -convergence. Oudet and Santambrogio [6] presented the Modica–Mortola approximation for branched transport. Conti et al. [7] investigated elastic shape optimization. Pegon et al. [8] studied fractal shape optimization in branched transport. Kang et al. [9] proposed a new clustering model using regularized k-means. Furthermore, there are numerous studies addressing image processing based on partial differential equations (PDEs) using the variational method [10–15]. Li [16] proposed a new multiphase image segmentation considering the images' morphological diversity. In [17], the authors introduced a new image segmentation method using multiphase segmentation based on binary image segmentation. Hu et al. [18] presented the minimum barrier superpixel segmentation which is capable of achieving cutting-edge performance. Liu et al. [19] proposed a graph-cut-based minimization method for image segmentation. The authors in [20] proposed a parametric snake model for image segmentation. Image segmentation

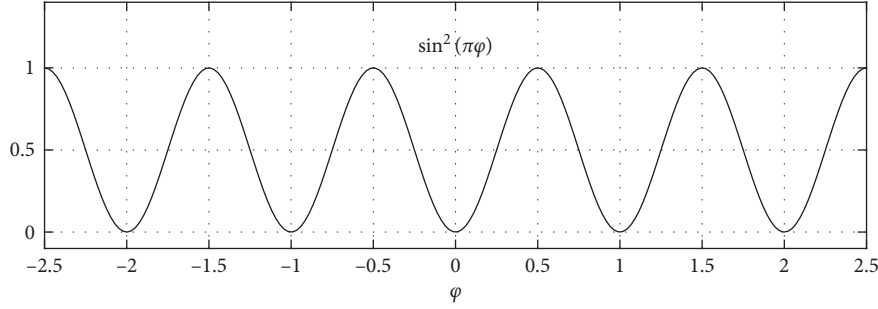


FIGURE 1: Multiple periodic well potential  $(1/\varepsilon)\sin^2(\pi\phi)$ . Here,  $\varepsilon = 1$  is used.

methods based on fractional calculus are popular emerging methods [21, 22]. Recently, deep learning-based segmentation methods have been actively studied in the image segmentation [23–26].

Several research studies have been conducted for multiphase image segmentation. Inspired by the work of Jung et al. [1], the authors in [27] presented a hybrid numerical method for multiphase image segmentation using a phase-field model. They used a periodic quartic polynomial instead of a sinusoidal function. A simplified Modica–Mortola functional was introduced for estimating piecewise-constant solutions for Fredholm integral equations of the first kind and a damped Newton method was employed to minimize the functional [28]. Huska et al. [29] presented an extension of the Mumford–Shah model for multiphase image segmentation using alternating directions methods of multipliers.

Most of the aforementioned methods use implicit schemes which update a solution by solving a discretized equation involving both the current state ( $n$  time level) of a given system and later one ( $n + 1$  time level). However, in this study, we propose an explicit segmentation scheme which directly updates the state of the given system at a later time level from the state of the system at the current time level without applying any iterative methods. The detailed process of the proposed explicit segmentation scheme is described in Section 3.3. The main purpose of this paper is to present a simple explicit numerical solution algorithm to the gradient flow for the Modica–Mortola functional.

This paper is organized as follows. In Section 2, we propose the numerical solution algorithm. In Section 3, we perform several characteristic numerical experiments to demonstrate the efficiency of the proposed numerical method. Finally, conclusions are provided in Section 5.

## 2. Numerical Solution Algorithm

We discretize equation (1) in two-dimensional space, i.e.,  $\Omega = (a, b) \times (c, d)$ . The one-dimensional case is defined in the same manner. Let  $N_x$  and  $N_y$  be positive integers,  $h = (b - a)/N_x$  be the uniform mesh size, and  $\Omega_h = \{(x_i, y_j): x_i = a + (i - 0.5)h, y_j = c + (j - 0.5)h, 1 \leq i \leq N_x, 1 \leq j \leq N_y\}$  be the discrete domain. Let  $\phi_{ij}^n$  be approximations of

$\phi(x_i, y_j, n\Delta t)$ , where  $\Delta t$  is the time step. Let  $\|\phi\|_2 = \sqrt{\sum_{i=1}^{N_x} \sum_{j=1}^{N_y} \phi_{ij}^2 / (N_x N_y)}$  be the discrete  $l_2$ -norm.

In [1], the authors developed a convex-splitting algorithm for minimization of the nonconvex energy functional. We propose the following operator splitting method (OSM) [30] for equation (1). Let us rewrite equation (1) as

$$\frac{\partial \phi(\mathbf{x}, t)}{\partial t} = f_1(\phi(\mathbf{x}, t)) + f_2(\phi(\mathbf{x}, t)), \quad (3)$$

where  $f_1(\phi(\mathbf{x}, t)) = 2\varepsilon\Delta\phi(\mathbf{x}, t)$  and  $f_2(\phi(\mathbf{x}, t)) = -(\pi/\varepsilon)\sin(2\pi\phi(\mathbf{x}, t))$ . Then, OSM is as follows: we solve equation (4) with  $\psi(\mathbf{x}, 0) = \phi(\mathbf{x}, n\Delta t)$  for a given value  $\phi(\mathbf{x}, n\Delta t)$  to get  $\psi(\mathbf{x}, \Delta t)$ .

$$\frac{\partial \psi(\mathbf{x}, t)}{\partial t} = f_1(\psi(\mathbf{x}, t)). \quad (4)$$

Next, using the solution obtained in the first step  $\psi(\mathbf{x}, \Delta t)$ , we solve equation (5) with  $\varphi(\mathbf{x}, 0) = \psi(\mathbf{x}, \Delta t)$  to get  $\varphi(\mathbf{x}, \Delta t)$ .

$$\frac{\partial \varphi(\mathbf{x}, t)}{\partial t} = f_2(\varphi(\mathbf{x}, t)). \quad (5)$$

Finally, we set  $\phi(\mathbf{x}, (n + 1)\Delta t) = \varphi(\mathbf{x}, \Delta t)$ . Now, we describe the above procedure in discrete approximation. First, we solve equation (4) using the explicit Euler method.

$$\frac{\phi_{ij}^* - \phi_{ij}^n}{\Delta t} = 2\varepsilon\Delta_h\phi_{ij}^n, \quad 1 \leq i \leq N_x, 1 \leq j \leq N_y, \quad (6)$$

where  $\Delta_h\phi_{ij}^n = (\phi_{i-1,j}^n + \phi_{i+1,j}^n - 4\phi_{ij}^n + \phi_{i,j-1}^n + \phi_{i,j+1}^n)/h^2$ . Here, the homogeneous Neumann boundary condition [31] is applied. Second, we solve equation (5) using the explicit Euler method.

$$\frac{\phi_{ij}^{n+1} - \phi_{ij}^*}{\Delta t} = -\frac{\pi}{\varepsilon}\sin(2\pi\phi_{ij}^*), \quad 1 \leq i \leq N_x, 1 \leq j \leq N_y. \quad (7)$$

For the stability of the scheme, we require a constraint for the time step. From equation (6), we have  $\Delta t < h^2/(8\varepsilon)$ . Because the right hand side term in equation (7) is periodic, we only need to check the stability with  $0 < \phi_{ij}^* < 0.5$ . More precisely, the sine function is  $2\pi$ -periodic while the sign is not important in the stability, and hence we only need to consider a half cycle. For this  $\phi_{ij}^*$ , we require  $0 < \phi_{ij}^{n+1} < \phi_{ij}^*$ . The inequality  $\phi_{ij}^{n+1} < \phi_{ij}^*$  is consistently satisfied for any  $\Delta t$ ,

as  $\sin(2\pi\phi_{ij}^*) > 0$  for  $0 < \phi_{ij}^* < 0.5$ . The inequality  $0 < \phi_{ij}^{n+1}$  implies

$$\Delta t < \frac{\varepsilon\phi_{ij}^*}{\pi \sin(2\pi\phi_{ij}^*)}, \quad (8)$$

which is a monotonically increasing function with respect to  $\phi_{ij}^*$  in  $(0, 0.5)$ . If we take limit as  $\phi_{ij}^* \rightarrow 0$  to the right hand side term in equation (8), then we obtain

$$\lim_{\phi_{ij}^* \rightarrow 0} \frac{\varepsilon\phi_{ij}^*}{\pi \sin(2\pi\phi_{ij}^*)} = \frac{\varepsilon}{2\pi^2}. \quad (9)$$

Therefore, we can assume the time step to be  $\Delta t = s \min[h^2/(8\varepsilon), \varepsilon/(2\pi^2)]$ , where  $0 < s < 1$  is a safety factor. For the one-dimensional case, we have  $\Delta t = s \min[h^2/(4\varepsilon), \varepsilon/(2\pi^2)]$ .

### 3. Numerical Experiments

In this section, we perform various numerical experiments to demonstrate the efficiency of the proposed method and to investigate the property of the gradient flow equation. We denote  $N$  as the number of iterations,  $h$  as the size of spatial step, and  $\Delta t$  as the time step scale. We terminate the main loop whence the discrete  $l_2$ -norm of the relative difference between two consecutive solutions is less than a given tolerance level, i.e.,

$$\frac{1}{N_x N_y} \sum_{i,j} \left| \frac{\phi_{ij}^n - \phi_{ij}^{n+1}}{\phi_{ij}^n} \right| < \text{tol}, \quad (10)$$

for some  $n$ . Here, all the numerical experiments are conducted on 2.70 GHz CPU and 4 GB DDR4 memory. We employ MATLAB R2019a as our test tool.

**3.1. Phase Evolution in One-Dimensional Computational Domain.** Unless specified otherwise, we fix  $h = 0.01$  in this section. Let  $\phi^\infty = \phi^{n+1}$  be taken as an equilibrium solution. We compute  $x_\alpha$  and  $x_\beta$  using a linear interpolation. For example,  $m$  depicts the index satisfying the condition  $\phi_m^\infty \leq 0.05 < \phi_{m+1}^\infty$ , such that  $x_\alpha = x_m + h(0.05 - \phi_m)/(\phi_{m+1} - \phi_m)$  is shown in Figure 2(a). Similarly,  $x_\beta$  can be obtained in a similar way. We define the transition thickness of  $\phi^\infty$  as  $L = x_\beta - x_\alpha$ , which is schematically illustrated in Figure 2(b). Here,  $\phi^\infty(x_\alpha) \approx 0.05$ , and  $\phi^\infty(x_\beta) \approx 0.95$ . Figure 2(c) shows the numerical steady states with different  $\varepsilon = 2h, 4h, \dots, 20h$  values. The initial condition in the computational domain  $\Omega = (0, 1)$  is  $\phi(x, 0) = 0$  if  $x < 0.5$ , and  $\phi(x, 0) = 1$  otherwise. The tolerance  $\text{tol} = 1 \text{ e-}16$  is used.

Table 1 lists the thickness ( $L = x_\beta - x_\alpha$ ) of the interface transition layer for various  $\varepsilon$  values.

Figure 3 shows the transition thickness  $L = x_\beta - x_\alpha$  against  $\varepsilon$ . We observe the linear relationship between  $L$  and  $\varepsilon$ . Fitting the data with a linear function, we have

$$\varepsilon(L) = 0.6158L + 0.0004. \quad (11)$$

Note that we employ the linear regression based on the least-squares method in order to find such a linear function.

Therefore, if we want to have  $L$  as the interface thickness, then we can use equation (11) to define the value of  $\varepsilon$ .

Figure 4 shows the numerical steady states with initial conditions  $\phi(x, 0) = 0$  if  $x < 0.5$ , and  $\phi(x, 0) = m$  otherwise. Figures 4(a), 4(b), 4(c), and 4(d) are the results with  $m = 1, 2, 3$ , and 4, respectively.  $\varepsilon = \varepsilon(4h)$ ,  $\text{tol} = 1 \text{ e-}16$ , and  $\Delta t$  with  $s = 0.1$  are used.

Figure 5 shows the numerical steady states with initial conditions  $\phi(x, 0) = 0$  if  $x < 0.5$ , and  $\phi(x, 0) = m$  otherwise. Figures 5(a), 5(b), 5(c), and 5(d) are the results with  $m = 1, 2, 3$ , and 4, respectively.  $\varepsilon = \varepsilon(8h)$ ,  $\text{tol} = 1 \text{ e-}16$ , and  $\Delta t$  with  $s = 0.1$  are used. Compared to the case with  $\varepsilon = \varepsilon(4h)$ , the width of the transition layer is larger in the results with  $\varepsilon = \varepsilon(8h)$ .

Figure 6 shows the temporal evolution of  $\phi$  with an initial condition on a computational domain  $\Omega = (0, 1)$ :

$$\phi(x, 0) = 2\text{rand}(x) + 5(x - 0.5), \quad (12)$$

where  $\text{rand}(x)$  is a random number between  $-1$  and  $1$ . The parameters  $h = 0.01$ ,  $\varepsilon = \varepsilon(4h)$ , and  $\Delta t$  with  $s = 0.1$  are used. In Figure 6, the dotted, solid, and thick solid lines are the initial profile, intermediate, and final solution after 100 iterations, respectively. While initial profile and intermediate solutions have random values, we can observe some flat regions with integer values at the final solution.

**3.2. Phase Evolution in Two-Dimensional Computational Domain.** In this section, we begin our experiment in a two-dimensional computational domain defined by  $\Omega = (0, 1) \times (0, 1)$ . To illustrate the robustness of the proposed model, Figure 7 shows the temporal evolution of  $\phi$ : Figures 7(a), 7(b), and 7(c) are snapshots at  $t = 0, \Delta t$ , and  $7\Delta t$ , respectively. The initial condition in  $\Omega$  is given by

$$\phi(x, y, 0) = 0.5\text{rand}(x, y) + 5(x + y - 1), \quad (13)$$

where  $\text{rand}(x, y)$  is a random number between  $-1$  and  $1$ .  $\varepsilon = \varepsilon(2h)$  and  $\Delta t$  with  $s = 0.99$  are used.

Figure 8 shows the temporal evolution of  $\phi$ : Figures 8(a), 8(b), and 8(c) represent snapshots at  $t = 0, \Delta t$ , and  $4\Delta t$ , respectively. The initial condition is defined by perturbed integers from 0, 1, 3, and 6 in 2 by 2 subdomains of  $\Omega$ . The maximum amplitude of the random number is 0.5.  $\varepsilon = \varepsilon(2h)$  and  $\Delta t$  with  $s = 0.99$  are used.

In addition, we investigate the same problem in Figure 8 with different  $s$  values to examine the effect of the safety factor  $s$ . Figure 9 shows the temporal evolutions of  $\phi$  with  $s = 0.11$ . Compared to the previous result, a small value of  $s$  brings out the small time step; hence, it takes a long computational time. Therefore, one might use the value of  $s$  as large as possible that is guaranteed to converge in order to gain fast convergence.

For the next step, we perform a test with a large variation of  $\phi$  and a larger value of  $s$ . Figure 10 shows the temporal evolution of  $\phi$ : Figures 10(a), 10(b), and 10(c) are snapshots at  $t = 0, \Delta t$ , and  $2\Delta t$ , respectively. The initial condition is defined by perturbed random integers between 0 and 26 in 5 by 5 subdomains of  $\Omega$ . The maximum amplitude of the random number is 0.5. The space step  $h = 0.01$ ,  $\varepsilon = \varepsilon(2h)$ ,

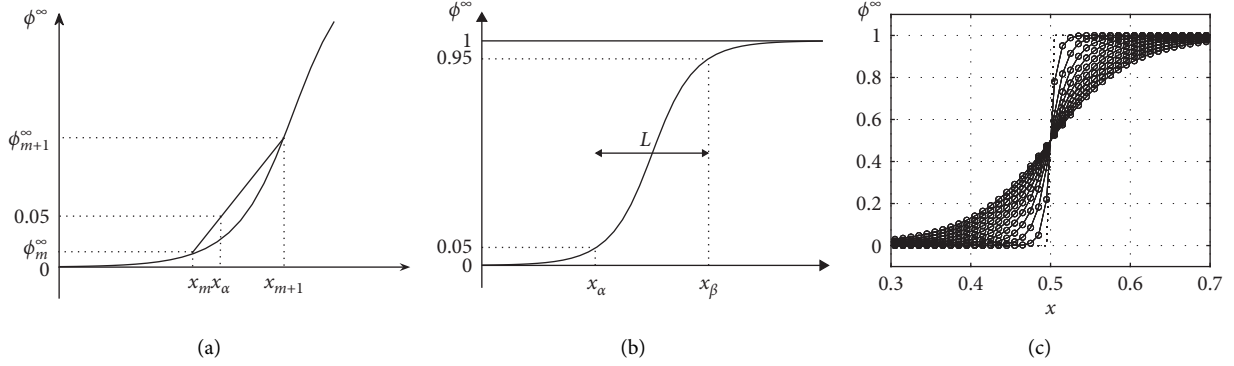


FIGURE 2: (a) Schematic illustration of linear interpolation evaluating  $x_\alpha$ . (b) Schematic illustration of transition thickness,  $L = x_\beta - x_\alpha$ . (c) Equilibrium solutions with different  $\epsilon = 2h, 4h, \dots, 20h$  values.

TABLE 1: Thickness ( $L = x_\beta - x_\alpha$ ) of interface transition layer for various  $\epsilon$  values.

Case	$\epsilon = 2h$	$\epsilon = 4h$	$\epsilon = 6h$	$\epsilon = 8h$	$\epsilon = 10h$
$L$	2.9903 $h$	6.5364 $h$	9.7668 $h$	12.9192 $h$	16.2230 $h$
Case	$\epsilon = 12h$	$\epsilon = 14h$	$\epsilon = 16h$	$\epsilon = 18h$	$\epsilon = 20h$
$L$	19.4323 $h$	22.6640 $h$	25.9192 $h$	29.1198 $h$	32.3832 $h$

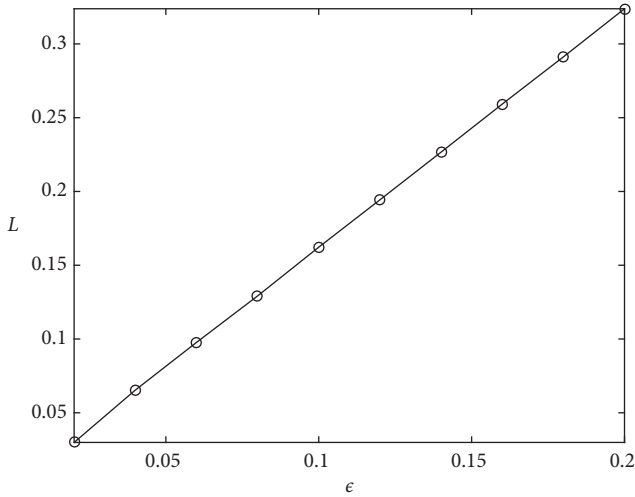


FIGURE 3: Plot of interface transition thickness  $L = x_\beta - x_\alpha$  with respect to  $\epsilon$ .

and  $\Delta t$  with  $s = 0.99$  are used. Even though we use a large value of  $s = 0.99$ , which is close to the critical value to the numerical stability, we have a good result. Furthermore, we get Figure 10(c) only after 2 iterations.

**3.3. Image Segmentation Application.** Image segmentation plays a significant role in image unperceiving, computer vision, medical image processing, and pattern identification [32–36]. We want to partition an image into several regions and make each region have characteristics such as edges, color, and object. The segmentation results are mainly for better analysis and meaningful interpretation of images. In this section, we apply

our method to multiphase image segmentation with a data-fitting term. We assume that there are  $K + 1$  phase fields for minimization of the following Mumford–Shah energy functional based on the Modica–Mortola functional:

$$\mathcal{E}(\phi) = \int_{\Omega} \left( \epsilon |\nabla \phi|^2 + \frac{1}{\epsilon} \sin^2(\pi \phi) + G_K(\phi, f_0) \right) dx. \quad (14)$$

The first term  $\epsilon |\nabla \phi|^2$  makes a smooth transition between phases and penalizes a large amount of oscillation. The reason is that minimizing the square of the gradient indicates a diffusion phenomenon and restricts sudden gradient changes, that is, the oscillation is suppressed because a large amount of sharp interface disappears. The second term represents a multiple periodic well potential, which derives the phase-field variable  $\phi$  to the closest integer value. Note that the reason for using the periodic function as a nonlinear reaction term unlike other models such as Mumford–Shah, Chan–Vese, and other snake contour-based methods is that the multiphase separation based on the multiple periodic well potential can be performed with single-order parameter. The third term is a fitting term, which is defined as follows:

$$G_K(\phi, f_0) = \frac{\lambda}{2} \sum_{k=0}^K (C_k - f_0)^2 \text{sinc}^2(\phi - k), \quad (15)$$

where  $f_0$  is the given image,  $\lambda$  is a positive parameter which indicates degree of fidelity, and  $C_k$  is the average of  $f_0$  in the  $k$ -level, where  $k = 0, 1, \dots, K$ , i.e.,

$$C_k = \frac{\int_{\Omega} f_0(\mathbf{x}) \text{sinc}^2(\phi(\mathbf{x}) - k) dx}{\int_{\Omega} \text{sinc}^2(\phi(\mathbf{x}) - k) dx}. \quad (16)$$

Note that as the value of  $\lambda$  increases, the influence of the edge-stopping function  $G_K$  becomes stronger, and the tendency to regress to the boundary of the original image becomes stronger.

Here,  $\text{sinc}(\phi) = \sin(\pi \phi) / (\pi \phi)$ , which is plotted by solid line in Figure 11, and the dashed line represents function  $\text{sinc}^2(\phi)$ . Note that the square of the  $\text{sinc}(\phi)$  plays the same role as the delta function in  $k$ -level.

Subsequently, we obtain the following gradient descent flow equation:

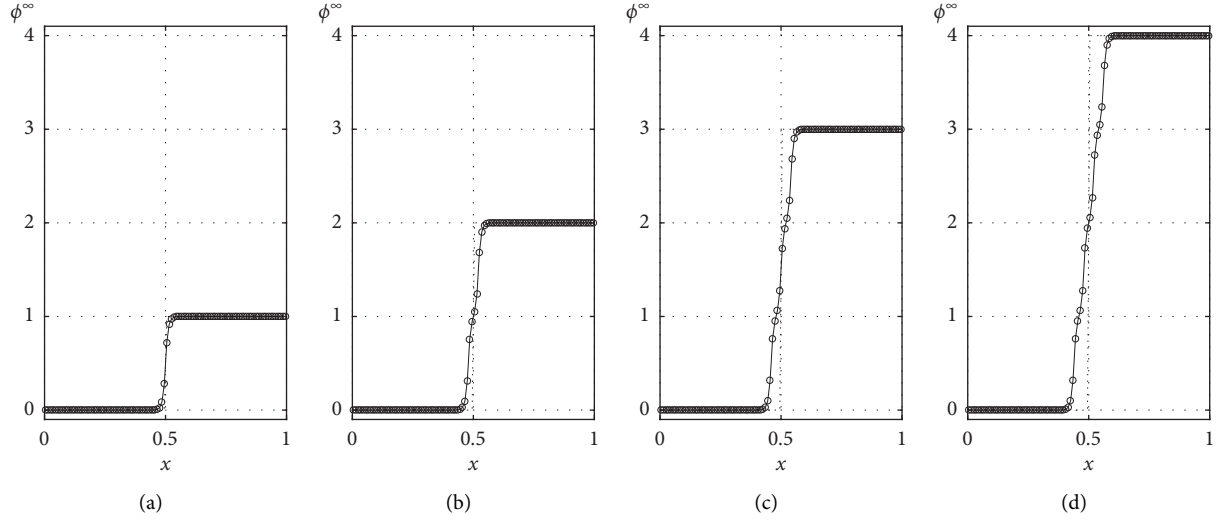


FIGURE 4: Numerical steady states with initial conditions  $\phi(x, 0) = 0$  when  $x < 0.5$ , and  $\phi(x, 0) = m$  otherwise. (a), (b), (c), and (d) are the results with  $m = 1, 2, 3$ , and  $4$ , respectively.  $\varepsilon = \varepsilon(4h)$  is used.

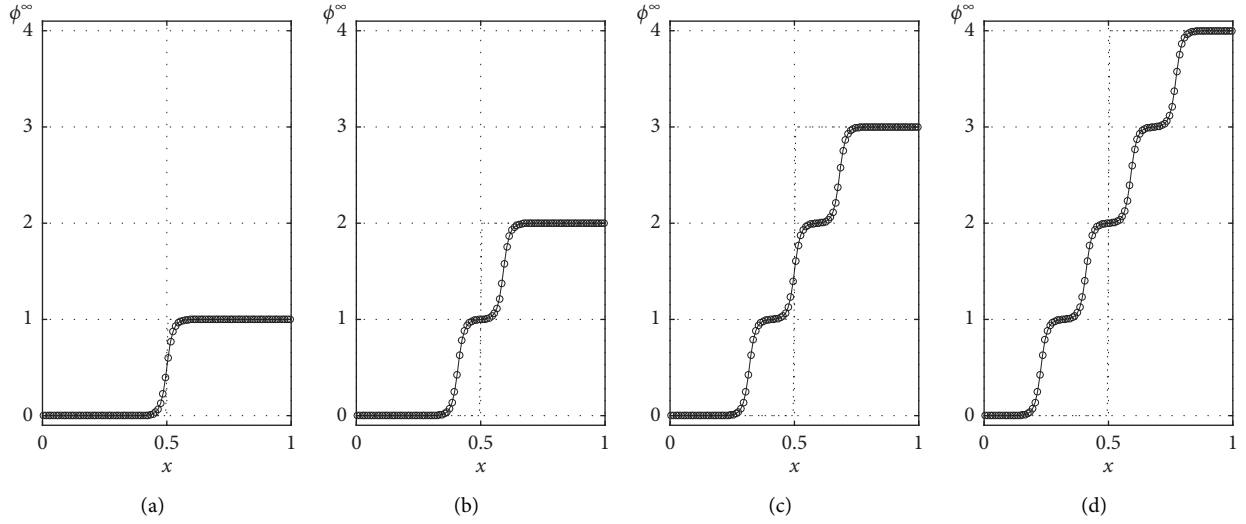


FIGURE 5: Numerical steady states with initial conditions  $\phi(x, 0) = 0$  when  $x < 0.5$ , and  $\phi(x, 0) = m$  otherwise. (a), (b), (c), and (d) are the results with  $m = 1, 2, 3$ , and  $4$ , respectively.  $\varepsilon = \varepsilon(8h)$  is used.

$$\begin{aligned} \phi_t &= 2\varepsilon\Delta\phi - \frac{\pi}{\varepsilon}\sin(2\pi\phi) \\ &\quad - \lambda \sum_{k=0}^K (C_k - f_0)^2 \left( \frac{\sin(2\pi(\phi - k))}{2\pi(\phi - k)^2} - \frac{\sin^2(\pi(\phi - k))}{\pi^2(\phi - k)^3} \right), \end{aligned} \quad (17)$$

where we assume that  $C_k$  is constant.

We present the operator splitting numerical algorithm to solve the proposed model. We split the original equation (17) into the following three equations:

$$\begin{aligned} \frac{\partial\phi(\mathbf{x}, t)}{\partial t} &= -\lambda \sum_{k=0}^K (C_k - f_0)^2 \\ &\quad \times \left( \frac{\sin(2\pi(\phi(\mathbf{x}, t) - k))}{2\pi(\phi(\mathbf{x}, t) - k)^2} - \frac{\sin^2(\pi(\phi(\mathbf{x}, t) - k))}{\pi^2(\phi(\mathbf{x}, t) - k)^3} \right), \end{aligned}$$

$$\frac{\partial\phi(\mathbf{x}, t)}{\partial t} = -\frac{\pi}{\varepsilon}\sin(2\pi\phi(\mathbf{x}, t)),$$

$$\frac{\partial\phi(\mathbf{x}, t)}{\partial t} = 2\varepsilon\Delta\phi(\mathbf{x}, t).$$

(18)

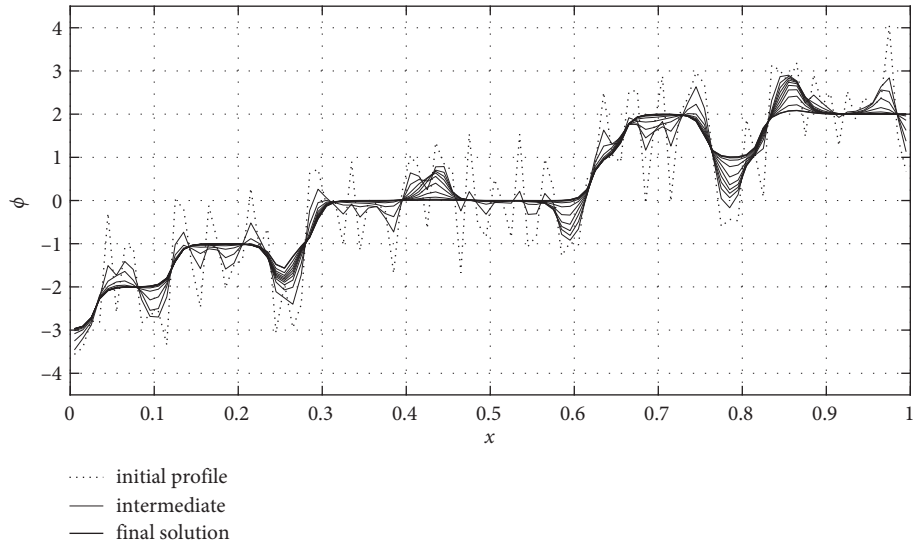


FIGURE 6: Temporal evolution of numerical solutions with initial condition,  $\phi(x, 0) = 2\text{rand}(x) + 5(x - 0.5)$ .

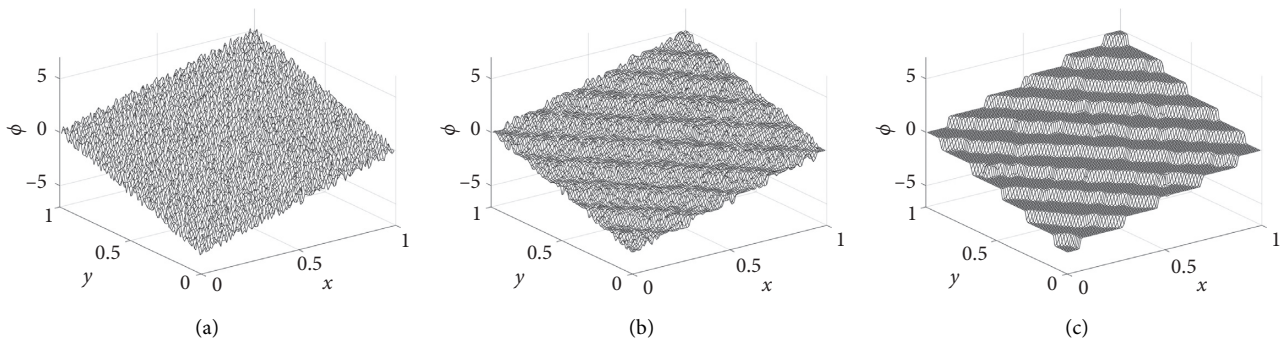


FIGURE 7: Temporal evolution of numerical solution: (a), (b), and (c) represent snapshots at  $t = 0, \Delta t$ , and  $7\Delta t$ , respectively.

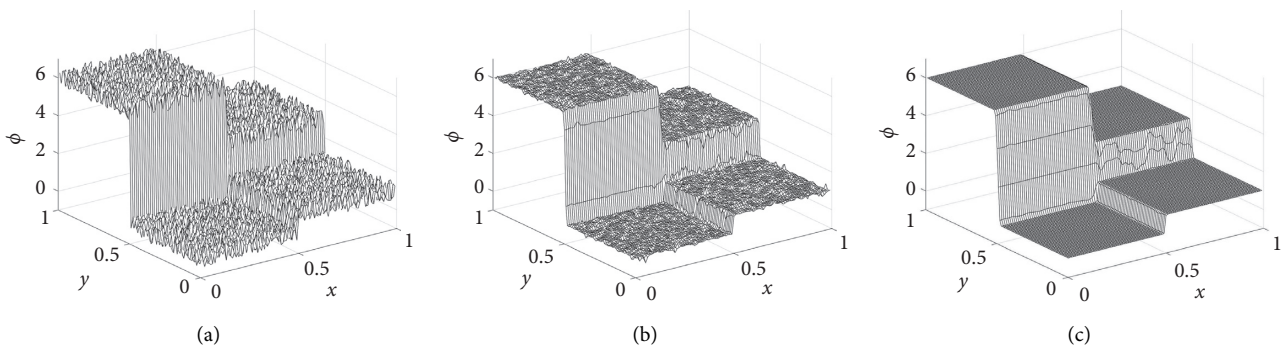


FIGURE 8: Temporal evolution of  $\phi$  with  $s = 0.99$ : (a), (b), and (c) are snapshots at  $t = 0, \Delta t$ , and  $4\Delta t$ , respectively.

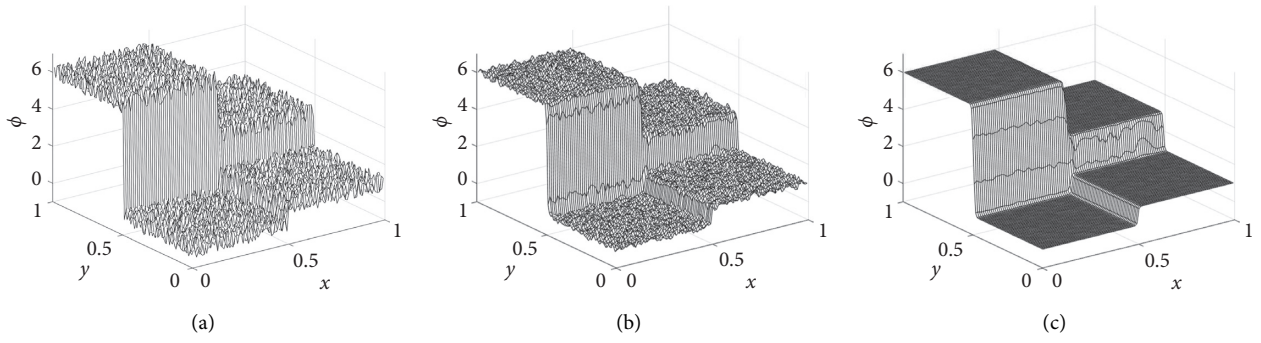


FIGURE 9: Temporal evolution of  $\phi$  with  $s = 0.11$ : (a), (b), and (c) are the snapshots at  $t = 0, 9\Delta t,$  and  $36\Delta t,$  respectively.

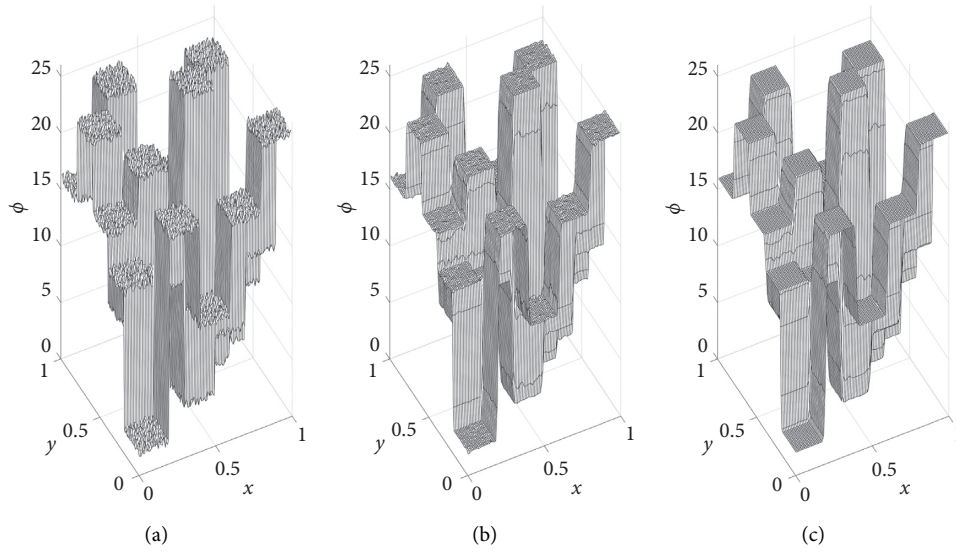


FIGURE 10: Temporal evolution of  $\phi$ : (a), (b), and (c) are snapshots at  $t = 0, \Delta t,$  and  $2\Delta t,$  respectively.

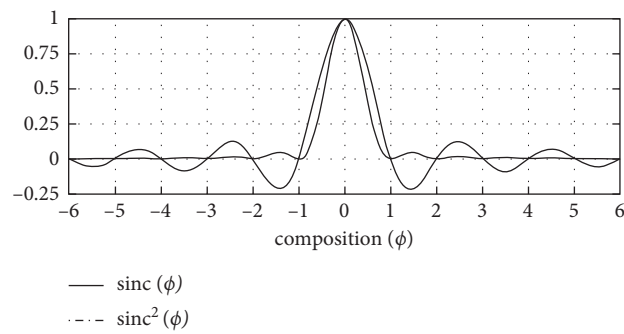


FIGURE 11: Functions  $\text{sinc}(\phi)$  and  $\text{sinc}^2(\phi)$ .

First, we solve the above three equations by applying the fully explicit method with a known value  $\phi^n$ , that is,

$$\frac{\phi_{ij}^{n+1/3} - \phi_{ij}^n}{\Delta t} = -\lambda \sum_{k=0}^K (C_k^n - f_{0,ij})^2 \times \left( \frac{\pi(\phi_{ij}^n - k) \sin(2\pi(\phi_{ij}^n - k)) - 2 \sin^2(\pi(\phi_{ij}^n - k))}{2\pi^2(\phi_{ij}^n - k)^3 + \delta} \right), \quad (19)$$

$$\frac{\phi_{ij}^{n+2/3} - \phi_{ij}^{n+1/3}}{\Delta t} = -\frac{\pi}{\varepsilon} \sin(2\pi\phi_{ij}^{n+1/3}), \quad (20)$$

$$\frac{\phi_{ij}^{n+1} - \phi_{ij}^{n+2/3}}{\Delta t} = 2\varepsilon\Delta_h\phi_{ij}^{n+2/3}, \quad (21)$$

where we added a small value  $\delta$  in the denominator to avoid singularities.

Note that if we replace  $\phi_{ij}^{n+1}$  by  $\phi_{ij}^{n+2/3}$  on the right side of equation (21), it becomes an implicit method, which generally needs an iterative method to solve it.

Now  $C_k^n$  is defined as follows:

$$C_k^n = \frac{\sum_{i=1}^{N_x} \sum_{j=1}^{N_y} f_{0,ij} \text{sinc}^2(\phi_{ij}^n - k)}{\sum_{i=1}^{N_x} \sum_{j=1}^{N_y} \text{sinc}^2(\phi_{ij}^n - k)}. \quad (22)$$

In the numerical experiments of image segmentation, we normalize the selected image  $f$  as  $f_0 = f - f_{\min}/f_{\max} - f_{\min}$ , where  $f_{\min}$  and  $f_{\max}$  are the minimum and maximum values of the selected image, respectively. For the initial phase-field value, we use the following formula:

$$\phi_{ij}^0 = n - 1 + \frac{f_{0,ij} - T_{n-1}}{T_n - T_{n-1}}, \quad \text{if } f_{0,ij} \in [T_{n-1}, T_n], \quad (23)$$

where  $T_n$  for  $n = 0, 1, \dots, N$  are target levels of the image. For example, if we have four target values,

$T_0 = 0, T_1 = 0.3, T_2 = 0.8$ , and  $T_3 = 1$ , then we have the initial phase-field value as illustrated in Figure 12. Note that the target values can be randomly selected; however, selecting them according to the distribution of the gray scale of the image ensures fast convergence. As our proposed method involves first observing the image and determining the target values, it is intuitive to follow the distribution of the gray scale of the image. Manual target selection [37–39] is a traditional method and has been used so far.

**3.4. Synthetic Image 1.** We test image segmentation using the image with 5 phases of  $240 \times 240$  mesh size [40]. We fix  $\text{tol} = 1 \text{e-}7$  unless otherwise specified. Figure 13 shows the image segmentation using uniformly distributed 5 target values. Here,  $s = 0.99$ ,  $h = 1/240$ ,  $\varepsilon = \varepsilon(2h)$ ,  $\lambda = 10$ , and  $\Delta t = s \min[h^2/(8\varepsilon), \varepsilon/(2\pi^2)]$  are used. Additionally, we use 5 target values:  $T_0 = 0, T_1 = 0.25, T_2 = 0.5, T_3 = 0.75$ , and  $T_4 = 1$ . We evaluate the discrete value of the Mumford–Shah energy functional as follows:

$$E(\phi^n) = \sum_{i,j} \left( \varepsilon \left( \frac{(\phi_{i+1,j}^n - \phi_{ij}^n)^2 + (\phi_{i,j+1}^n - \phi_{ij}^n)^2}{h^2} \right) + \frac{1}{\varepsilon} \sin^2(\pi\phi_{ij}^n) + \frac{\lambda}{2} \sum_{k=0}^K (C_k^n - f_{0,ij})^2 \sin^2(\phi_{ij}^n - k) h^2 \right), \quad (24)$$

where  $C_k^n$  is described earlier in equation (22).

As shown in Figure 13(c), the synthetic image with 5 uniformly distributed target values is segmented to 5 phases. Moreover, we further consider a normalized ratio of  $\mathcal{E}(\phi^n)/\mathcal{E}(\phi^0)$  in the segmentation process. Figure 13(d) shows the energy plot  $\mathcal{E}(\phi^n)$ , and the criterion for convergence is  $n = 5$ , which is determined by  $|(\mathcal{E}(\phi^n) - \mathcal{E}(\phi^{n-1}))/\mathcal{E}(\phi^0)| < \text{tol}_e$ . This threshold  $\text{tol}_e$  is set equal to  $1\text{e-}4$  for the tests with the synthetic image unless otherwise specified. Therefore, numerical steady state is achieved at the intersection of two types of stopping criteria, relative consecutive errors, and normalized decaying energy ratios.

Note that the important point is that the target values are set as hyperparameters in the case of real image or automatically set through the distribution of gray-scale values of image. Therefore, uniformly distributed target values used in Figure 13 are nothing special, i.e., these can be nonuniformly distributed.

To illustrate the robustness of the proposed model with respect to noise, we conduct an image segmentation experiment for the 5% random noise from the uniform distribution added to the image at first. In this test, we choose the initial image with levels 0, 0.2, 0.4, 0.7, and 1. The image corrupted by 5% noise and the mesh plot of the image are shown in Figures 14(a) and 14(b), respectively. After 15



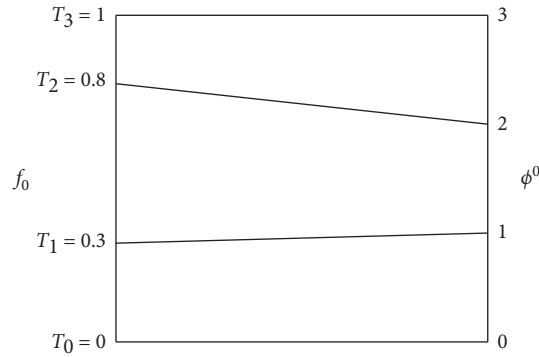


FIGURE 12: Initialization of multiphase image segmentation.

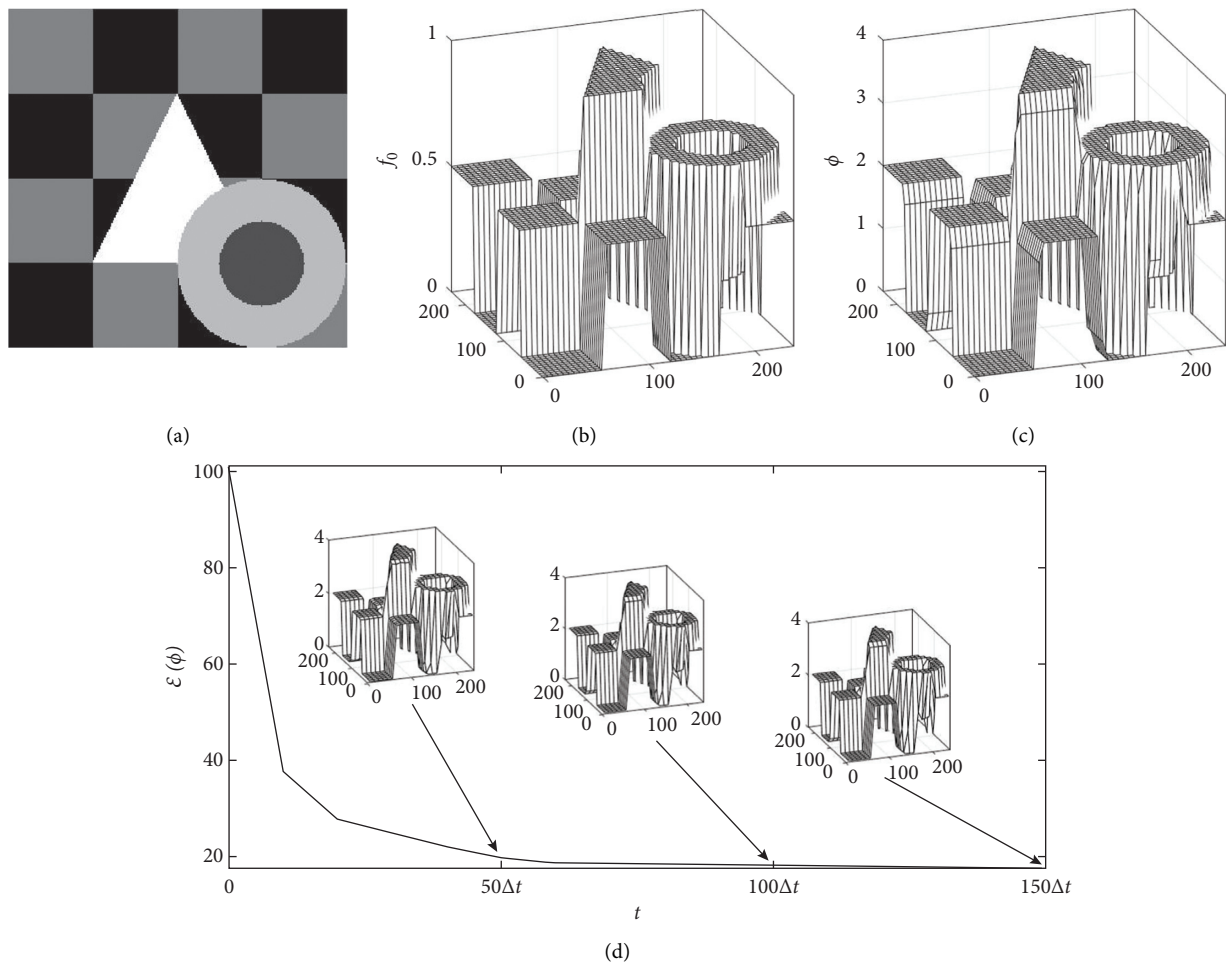


FIGURE 13: Image segmentation process with 5 phases. (a) Initial gray-scale image with 5 uniformly distributed target values. (b) Mesh plot of the initial image. (c) Converged phase field after 5 iterations. (d) Energy decrease plot and corresponding snapshots.

iterations, we confirm the converged phase field as shown in Figure 14(c) by using Figure 14(d). Compared to Figure 13(d), there is no significant difference in the degree of energy decaying; however, 10 more iterations are needed because the random noise is added, and therefore the convergence of relative consecutive errors takes more iterations relatively.

Subsequently, we generate a kind of impulsive noise, which is called salt and pepper noise, in the synthetic image. Figure 15 depicts the segmentation results with salt and pepper noise. Note that we change the corresponding values of parameters,  $s = 0.1$  and  $\lambda = 500$ , in this case.

Since relatively small  $s$  is used, the number of iterations has to increase to achieve a similar level of segmentation as

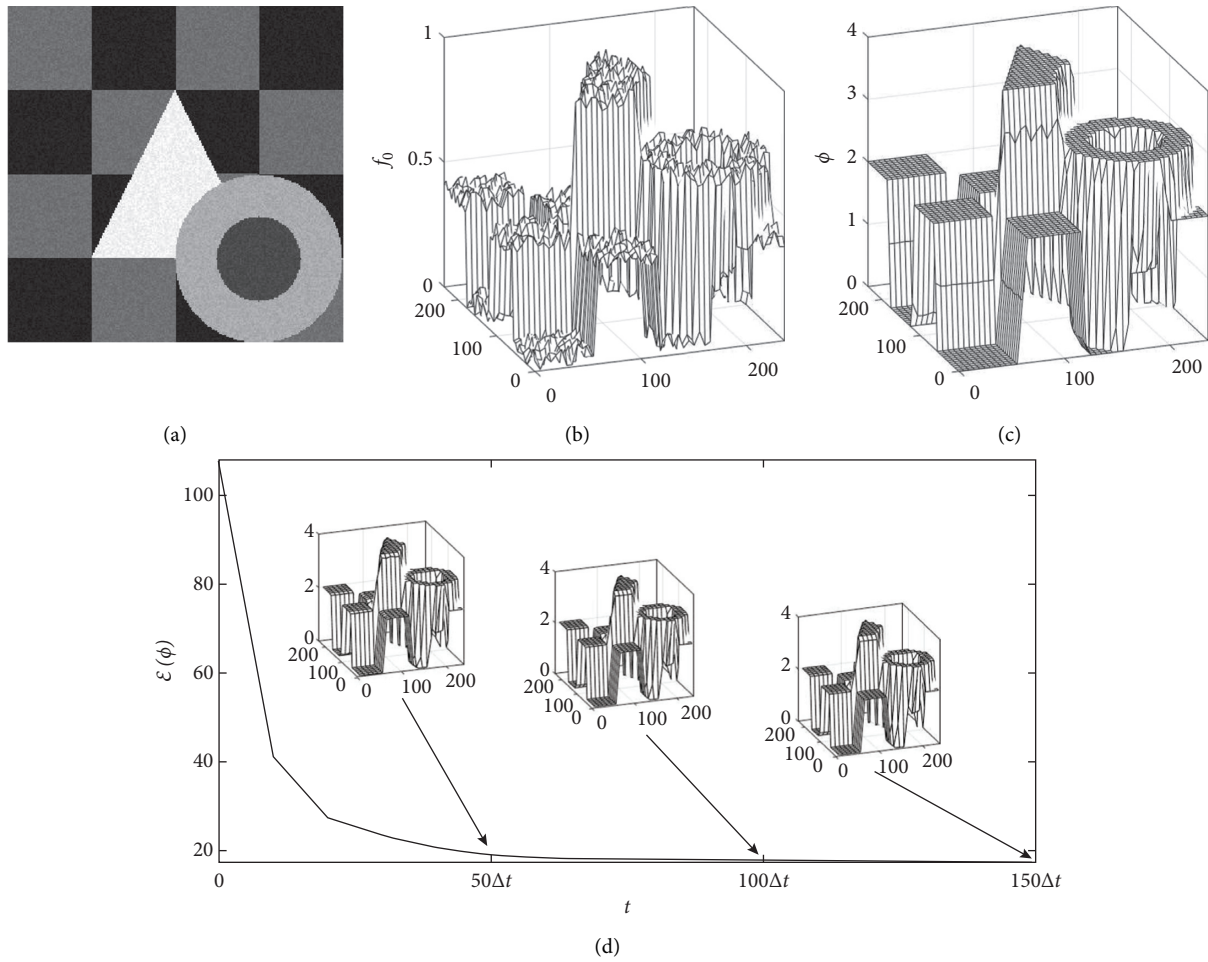


FIGURE 14: Image segmentation process of the noise-corrupted image with 5 phases. (a) Initial gray-scale image corrupted by 5% random noise from the uniform distribution with 5 nonuniformly distributed target values. (b) Mesh plot of the initial image. (c) Converged phase field after 15 iterations. (d) Energy decrease plot and corresponding snapshots.

shown in Figure 14. The value of  $s$  is concerned with the accuracy of solutions in this case, which is covered in more detail in the parameter test section below. The boundaries tend to be relatively smeared rather than the results of randomly perturbed noise image segmentation as shown in Figure 14. Another type of impulsive noise is anisotropic noise which is concentrated in specific area. In this case, we generate anisotropically the 20% random noise value from the standard normal distribution. Moreover, we conduct a similar examination for periodic noise. Figure 16 shows the segmentation results initially corrupted by anisotropic and periodic noises. For the anisotropic noise case, we adjust the target values since the specified areas occupy a small portion of the entire area, which implies that the outliers are scaled together when scaling process is done; hence, one may create a buffer as 0.2 to both sides, 0 and 1. We take 0.2, 0.35, 0.5, 0.65, and 0.8 as the target values. This is the reason why Figure 16(a) has a slightly different colormap from others in noise-corrupted images. We further change the value of fidelity,  $\lambda = 100$ , and the others are the same as those of salt and pepper noise case. On the other hand, we adopt the same target values described in Figure 14 for periodic noise case

and just vary the parameters  $s = 0.1$ ,  $\lambda = 10$ . Note that we omit mesh plots and energy plots since they are duplicated as the results listed in Figure 15.

As can be seen from the above results, the segmentation results using our proposed method are robust. Furthermore, we present the long time numerical energy stability for equations (19)–(21) in Figure 17. Here, we use all the same parameters listed above for Figure 14, but for the number of iterations to 500, the final time is  $T = 500\Delta t \approx 30.895$ .

According to Figure 17, our method has long-term energy stability, which asserts nonoscillation asymptotic behaviors.

Though a phase-field modeling itself does not include an optimizing algorithm, we examine the value of intersection over union (IoU) to measure the accuracy of segmentation. Figure 18 shows original and predicted bounding boxes with respect to different  $\epsilon$  values, and Table 2 lists the value of IoU for each case.

In this test, we use the parameter values  $s = 0.1$ ,  $\lambda = 100$ , and the others are the same as used in Figure 14. Note that  $\epsilon$  is concerned with transition width and the number of pixels in this image is 240 for each axis. Therefore, IoU might be

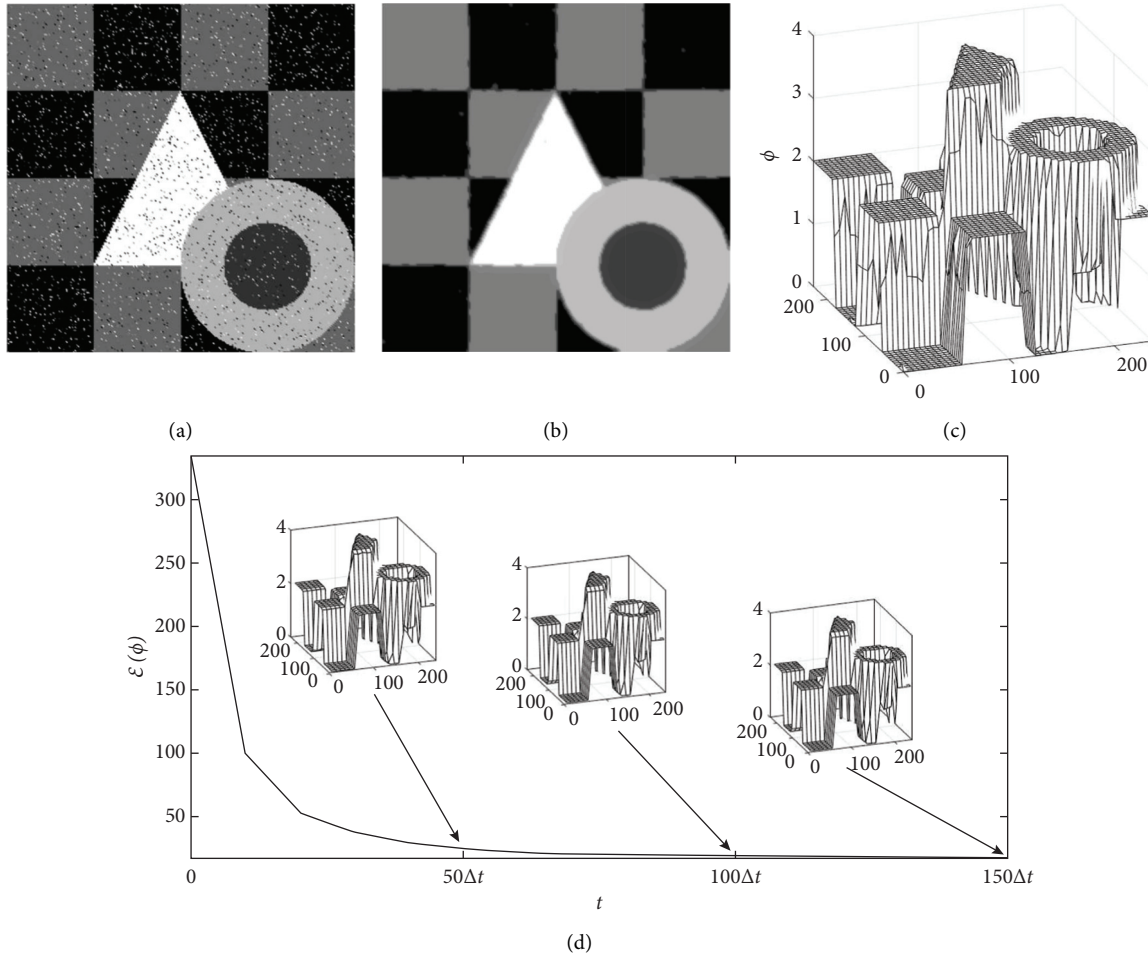


FIGURE 15: Image segmentation process of the noise-corrupted image with 5 phases. (a) Initial gray-scale image corrupted by salt and pepper noise with 5 nonuniformly distributed target values. (b) Segmented image after 150 iterations. (c) Converged phase field after 150 iterations. (d) Energy decrease plot and corresponding snapshots.

similar for  $\epsilon$  values exceeding a certain scale in diffuse-interface models due to the lack of the number of pixels. This is the reason why we have similar values for  $\epsilon(4h)$  and  $\epsilon(8h)$ .

Moreover, we verify the dullness of edge of our proposed method. Figure 19 shows the dullness of edge with respect to various  $\epsilon$  values. According to this result, the boundaries become smooth enough as  $\epsilon$  increases; it may result in a drawback such as a smeared boundary problem. The theoretical details of both diffuse-interface and sharp-interface limits can be checked in the following references [41, 42] and can be also found in the references therein.

**3.5. Complex Image.** For the following step, we use a more complex image. We fix  $\text{tol} = 1 \text{ e-}6$  and  $\text{tol}_\epsilon = 1 \text{ e-}4$  unless otherwise specified. We take a brain MRI image used in [43] as the first example. In medical science, there are cases in which diagnostic results are obtained by tracking and observing areas that have the same color in the image. Therefore, the brain MRI image is suitable for checking the performance of our method. We convert the brain MRI image to gray scale, which ranges from 0 to 1, and choose the pixels as target values  $T$  as our region of interest. Fast

convergence of the explicit scheme is therefore generally ensured, and one may not continuously select the pixels that have almost the same gray-scale distribution values in reality. If we want to segment regions of intensity at  $(i_k, j_k)$  for  $k = 0, 1, \dots, K$ , then we define  $C_k$  as the local mean of the near 8 cells and itself.

$$C_k = \frac{1}{9} \sum_{a,b=-1,0,1} f_{0,i_k+a,j_k+b} \quad (25)$$

Note that we fix these defined values until completion of the segmentation process. Here, we use  $s = 0.3$ ,  $h = 1$ ,  $\epsilon = \epsilon(2h)$ ,  $\lambda = 1$ ,  $\Delta t = s \min[h^2/(8\epsilon), \epsilon/(2\pi^2)]$ , and  $K = 3$ . The size of image is  $290 \times 320$ . Figures 20(a) and 20(b) show the original image and the image with  $C_k$  positions for  $k = 0, 1, 2, 3$ , respectively. Figures 20(c) and 20(d) show mesh plots of the original brain MRI and the segmented phase field, respectively. Figures 20(e)–20(h) show the sectional segmentation images for each  $k$ -level.

Note that the expression in black and white colors is just to clarify the visualization. Therefore, the gray texture in the image can be obtained in exactly the same way. Similarly, the numerical energy stability for the proposed method with

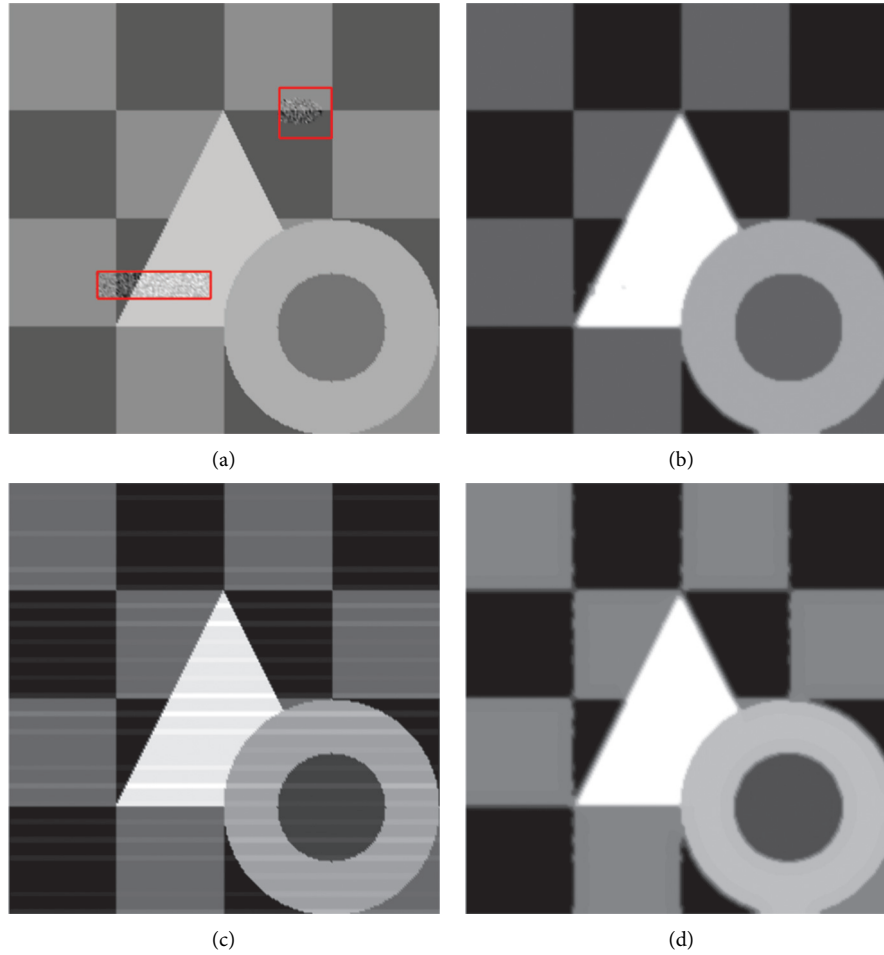


FIGURE 16: Image segmentation process of noise-corrupted image with 5 phases. (a) Initial gray-scale image anisotropically corrupted by 20% random noise from the standard normal distribution. We use 5 uniformly distributed target values with buffer. Note that the noise occurs in red boxes. (b) Segmented image after 150 iterations. (c) Initial gray-scale image corrupted by periodic noise with 5 nonuniformly distributed target values. (d) Segmented image after 150 iterations.

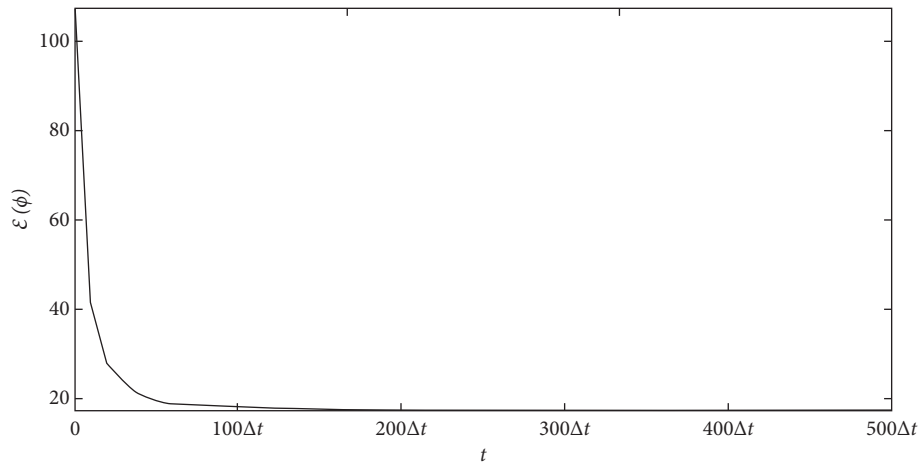


FIGURE 17: Energy plot of the Mumford–Shah energy functional obtained with proposed method equations (19)–(21) with the initial condition in Figure 14.

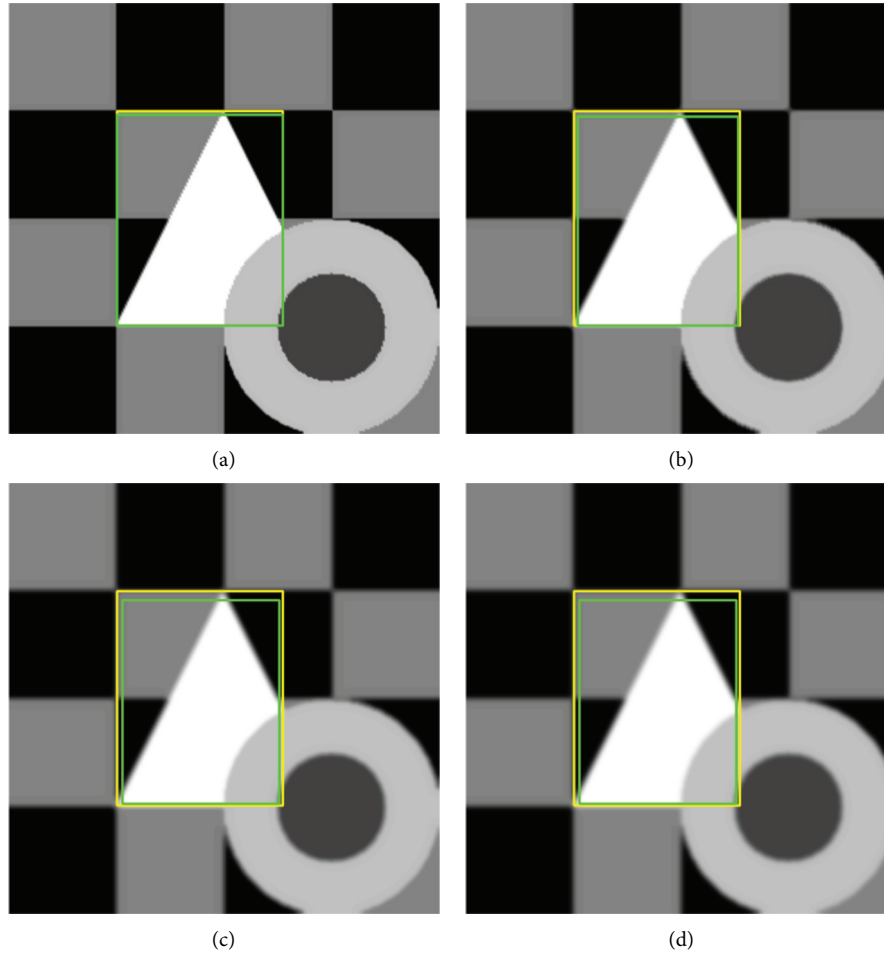


FIGURE 18: Bounding boxes of both original and segmented images: (a)  $\varepsilon = \varepsilon(h)$ , (b)  $\varepsilon = \varepsilon(2h)$ , (c)  $\varepsilon = \varepsilon(4h)$ , and (d)  $\varepsilon = \varepsilon(8h)$ . Note that the yellow boxes are original, and the green boxes are predicted.

TABLE 2: IoU for different  $\varepsilon$  values (note that the values are rounded up from the fifth decimal place).

$\varepsilon(H)$	$H = h$	$H = 2h$	$H = 4h$	$H = 8h$
IoU	0.9832	0.9430	0.8980	0.8980

local mean  $C_k$  is presented in Figure 21. Here, we use all the same parameters listed above for Figure 20, except for the number of iterations (500).

**3.6. Parameter Test.** We perform parameter tests on image with low contrast and high-level noise in this section. We employ the  $132 \times 641$  sized vertebral image listed in [44], which has low contrast near the boundaries of the object. We initially transform the image into gray scale and perturb with random noise about  $\pm 30\%$  within  $[-1, 1]$ . Figure 22 shows both original and noise perturbed vertebral MRI images.

We have targeted the spines within the image to segment, and  $K = 3$  is adopted for convenience. Recall that  $K$  is a hyperparameter, and hence there is an adequate value of  $K$  to achieve fast computation as well as the target values. We fix the default set of parameters as  $s = 0.6$ ,  $h = 0.1$ ,  $\lambda = 200$ ,

and  $\varepsilon = \varepsilon(12h)$ . Figure 23 depicts the effect of parameters. We set the tolerance levels for relative consecutive errors to  $\text{tol} = 1 \text{ e-}5$  and for normalized energy ratios to  $\text{tol}_e = 1 \text{ e-}3$ , respectively.

As depicted in Figures 23(a)–23(c), the details near the boundaries of object are captured as the value of  $s$  is small. Since  $s$  affects the scale of time step  $\Delta t$ , this numerical result of the dynamics of phase field with small value of  $s$  fits well with theoretical predictions. However, there is a drawback of segmenting the wrong areas around the boundaries of object if the noise is severe. The effect of space step  $h$  is shown in Figures 23(d)–23(f). It affects the time step size like  $s$ ; however, it simultaneously affects the value of  $\varepsilon$ . Since we analyzed theoretically the derivation of  $\varepsilon$  for  $h = 0.01$ , relatively large value of  $h$  leads to a torn segmented image. Figures 23(g)–23(i) illustrate the effect of  $\lambda$ . If  $\lambda$  is small, then the segmented image has a smeared boundary, while the image has a sharp interface with large value of  $\lambda$ . It implies that the fidelity force is dominant if the value of  $\lambda$  is large; therefore, unintended boundaries can be generated inside of object. Note that boundaries in phase-field models are represented by an average level of transition region. Therefore, these have sharp-interface limits asymptotically

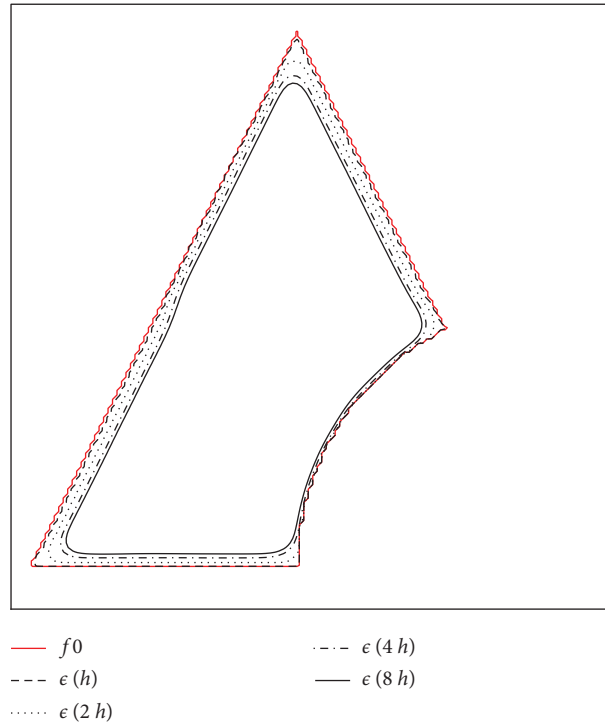


FIGURE 19: Dullness of edge of our proposed method with respect to  $\epsilon(m)$ , where  $m = h, 2h, 4h, 8h$ .

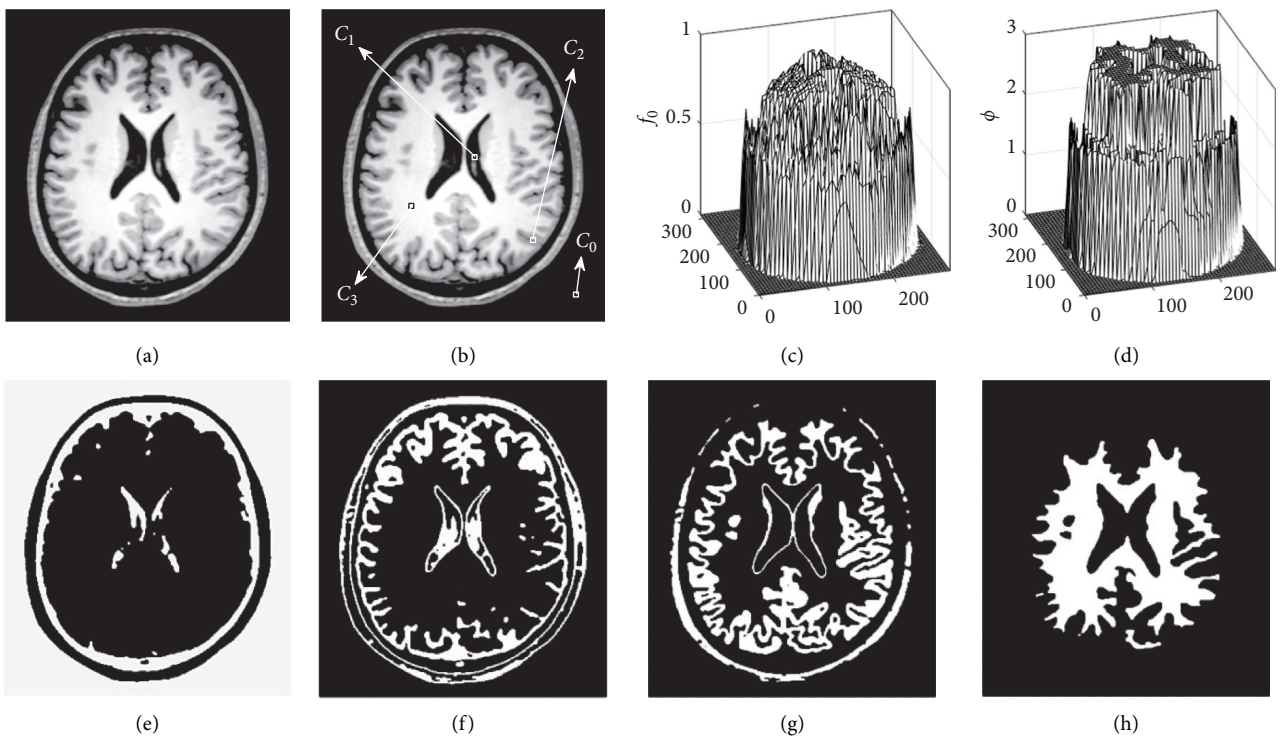


FIGURE 20: (a) Initial image of brain MRI. (b) Locations of  $C_k$  for  $k = 0, 1, 2, 3$ . (c) Mesh plot of initial image. (d) Segmentation results. Sectional image segmentation process of brain MRI: (e)  $\phi = 0$ , (f)  $\phi = 1$ , (g)  $\phi = 2$ , and (h)  $\phi = 3$ .

and are smoothly smeared. Figures 23(j)–23(l) describe the effect of  $\epsilon$ . The small value of  $\epsilon$  makes the transition width to be narrow, resulting in jagged edges due to inconsistent

separation depending on the shape of boundary while larger  $\epsilon$  values make the boundaries too smooth, making them more blunt than the actual shapes.

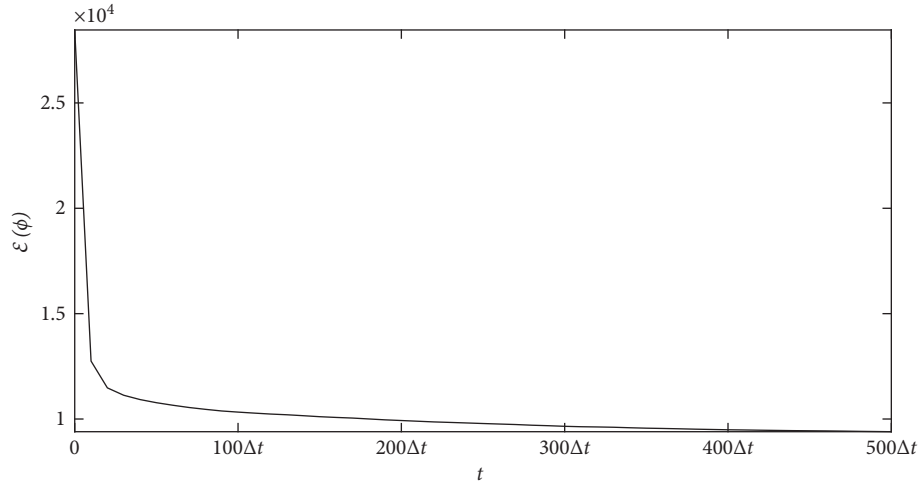


FIGURE 21: Energy plot of the Mumford–Shah energy functional using our proposed method with local mean  $C_k$ .

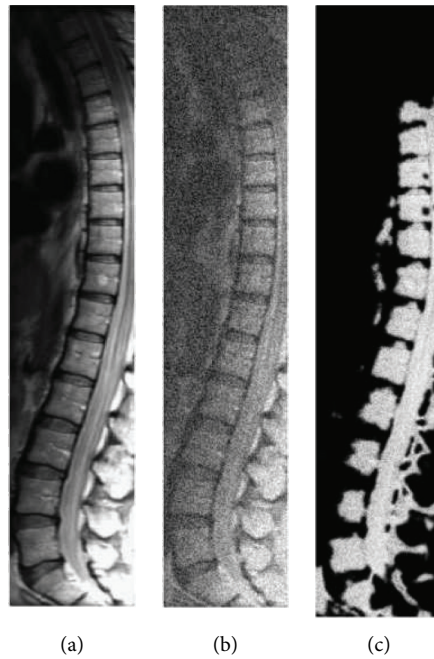


FIGURE 22: (a) Original image of vertebral MRI with low contrast near boundaries of object. (b) Perturbed image of vertebral MRI with  $\pm 30\%$  noise from the uniform distribution. (c) Segmented image using (b) with default parameters.

**3.7. Comparison Test.** We compare the segmented images followed by using different schemes with respect to the results followed by using our method in this section. Figure 24 shows the segmented images using our method and the methods listed in [27, 45]. For more detailed information on the methods, refer to [27, 45] and the references therein.

We adopt the parameters  $\epsilon = 0.01$ ,  $\Delta t = 0.25h^2$ , and  $\mu = 100$  for both quadratic regularization and superlinear models. As depicted in Figure 24, the segmented results using our proposed method do not differ significantly from the results using existing methods.

Furthermore, we compare the performance of our simple method to the implicit method used in [27] in terms

of the CPU time. We measured the elapsed time until both the stopping criteria are satisfied. Two different time step sizes are used:  $\Delta t = 0.5\epsilon/\pi^2 \approx 0.0187$  with a safety factor  $s = 0.3$  and  $\Delta t_{ref} = 1e-5$ . We fix  $\epsilon = \epsilon(2h)$  for both the schemes. We use the following initial value  $\phi^0$ ,  $\phi_{ij}^0 = Kf_{0,ij}$ , where  $K = 3, 4$  and target values as  $T_0 = 0.01, T_1 = 0.35, T_2 = 0.66, T_3 = 0.92$  in the case of  $K = 3$  and  $T_0 = 0.004, T_1 = 0.23, T_2 = 0.52, T_3 = 0.77, T_4 = 0.94$  in the case of  $K = 4$ . Here,  $K$  is the number as described in equation (15). Furthermore, we resize the size of image used in Figure 20 to  $256 \times 256$  since the reference method employs the multigrid method. Table 3 shows the result of the CPU time performance test. If we use  $\Delta t_{ref}$ , then we have similar CPU times for both the methods. However, if we use a larger time step, then the CPU time is

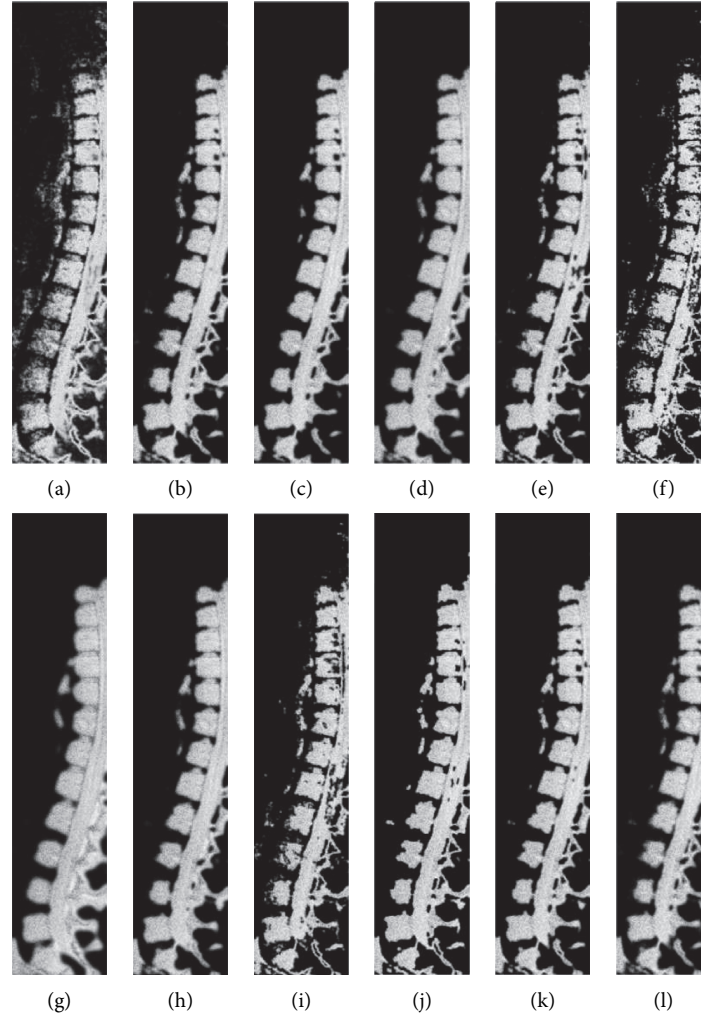


FIGURE 23: (a)–(c) verify the effect of  $s$  on the image segmentation. (d)–(f) verify the effect of  $h$  on the image segmentation. (g)–(i) verify the effect of  $\lambda$  on the image segmentation. (j)–(l) verify the effect of  $\epsilon$  on the image segmentation.

reduced by one order of magnitude. This result implies that we can achieve fast computation speed via the proposed method with the moderate time step proposed in Section 2.

#### 4. Geometric Active Segmentation

For approximation of the geometric active segmentation for multiphase image, the governing equation is given as follows:

$$\begin{aligned} \frac{\partial \phi(\mathbf{x}, t)}{\partial t} &= g(f_0(\mathbf{x})) \left( 2\epsilon \Delta \phi(\mathbf{x}, t) - \frac{\pi}{\epsilon} \sin(2\pi \phi(\mathbf{x}, t)) \right) \\ &\quad + \lambda g^2(f_0(\mathbf{x})) \phi(\mathbf{x}, t) \frac{1}{\epsilon} \sin^2(\pi \phi(\mathbf{x}, t)), \\ \mathbf{x} &\in \Omega, \quad 0 < t \leq T, \end{aligned} \quad (26)$$

where  $f_0(\mathbf{x})$  for  $\mathbf{x} = (x, y)$  is a given image,  $g$  is an edge-stopping function,  $\phi(\mathbf{x}, t)$  is an order parameter,  $\epsilon$  is a positive constant, and  $\lambda$  is a constant parameter.  $\Omega$ , in particular, is a domain bounded in  $\mathbb{R}^d$  ( $d = 1, 2$ ). Note that we restrict  $\phi(\mathbf{x}, t) \geq 0$  for convenience. In equation (26),  $g(f_0(\mathbf{x}))$  is the edge-stopping function and is defined as

$$g(f_0(\mathbf{x})) = \frac{1}{1 + |\nabla(G_\sigma * f_0)(\mathbf{x})|^p}, \quad (27)$$

where  $(G_\sigma * f_0)(\mathbf{x})$  is the convolution of the given image  $f_0$  and the Gaussian function

$$G_\sigma = \frac{1}{2\pi\sigma^2} e^{-x^2+y^2/2\sigma^2}. \quad (28)$$

Here, we will use  $p = 2$ . The function  $g(f_0(\mathbf{x}))$  is close to 1 in homogeneous regions and is close to 0, when the gradient of the image is large. We present the operator splitting numerical algorithm to solve the proposed model. We split the original equation (26) into the following three equations:



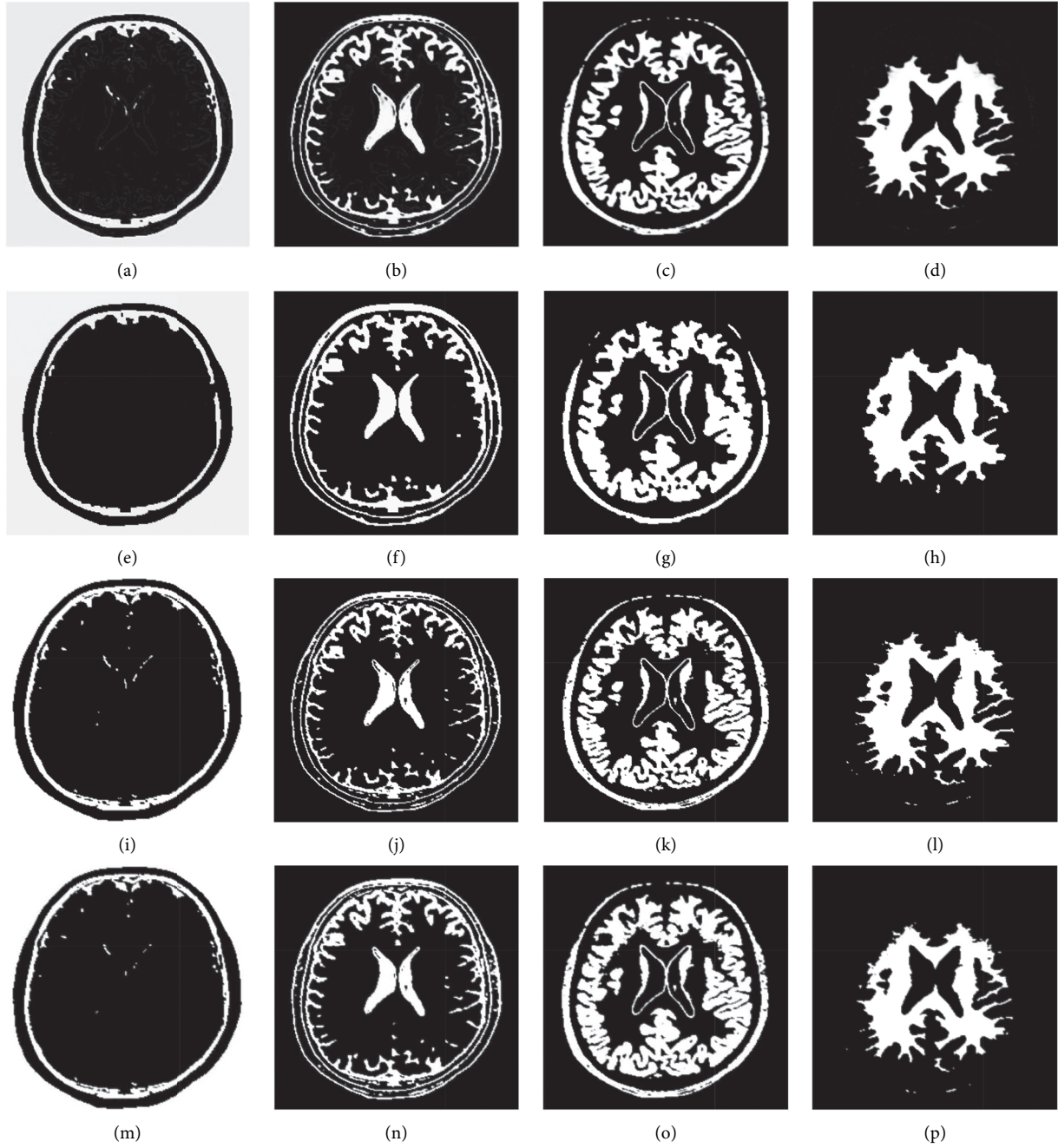


FIGURE 24: (a)–(d) Segmented images using our proposed method. (e)–(h) Segmented images using implicit method followed by Li and Kim [27]. (i)–(l) Segmented images using quadratic regularization method followed by Kang and March [45]. (m)–(p) Segmented images using the superlinear model followed by Kang and March [45].

$$\begin{aligned} \frac{\partial \phi(\mathbf{x}, t)}{\partial t} &= \lambda g^2(f_0(\mathbf{x})) \phi(\mathbf{x}, t) \frac{1}{\varepsilon} \sin^2(\pi \phi(\mathbf{x}, t)), \\ \frac{\partial \phi(\mathbf{x}, t)}{\partial t} &= -\frac{\pi}{\varepsilon} g(f_0(\mathbf{x})) \sin(2\pi \phi(\mathbf{x}, t)), \\ \frac{\partial \phi(\mathbf{x}, t)}{\partial t} &= 2\varepsilon g(f_0(\mathbf{x})) \Delta \phi(\mathbf{x}, t). \end{aligned} \quad (29)$$

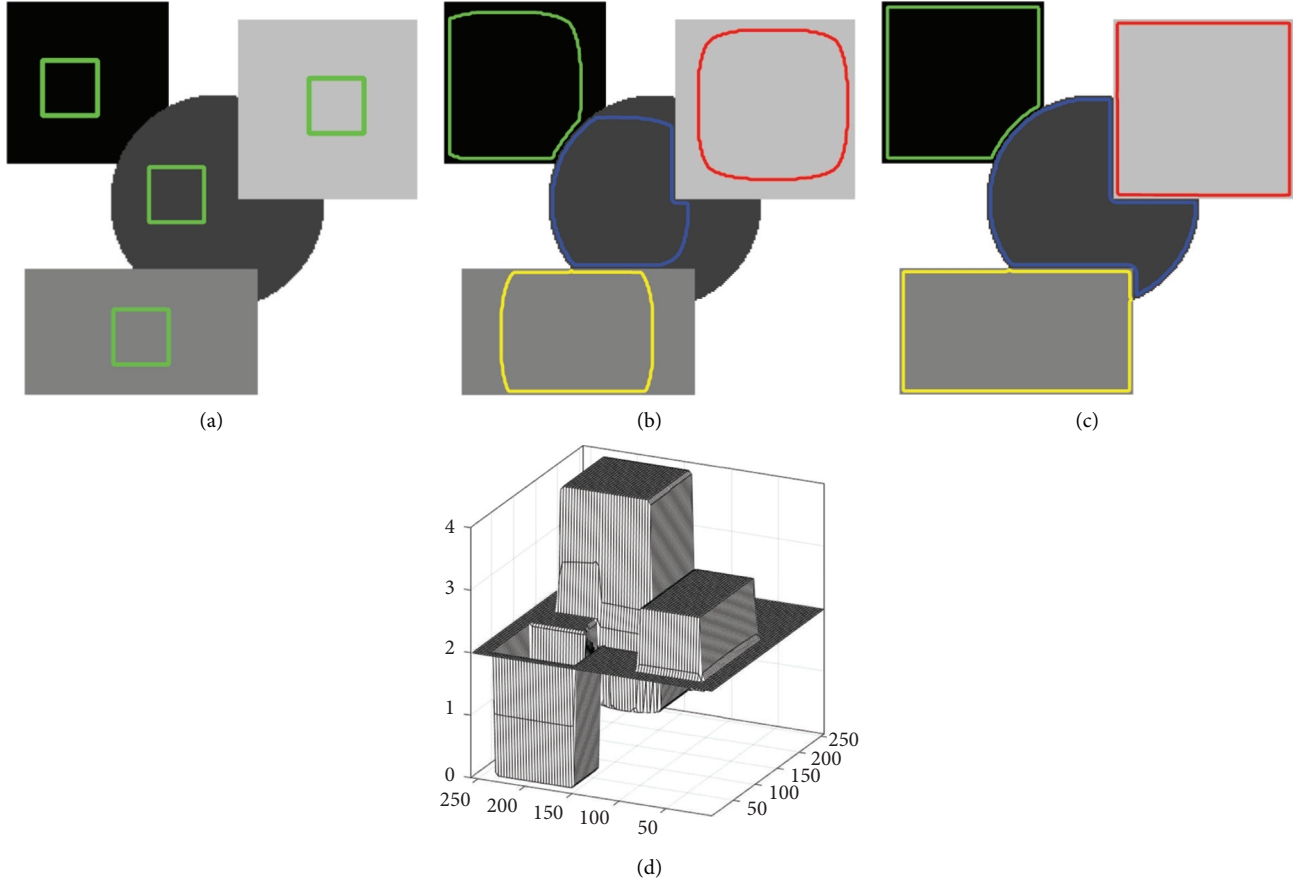
First, we solve the above three equations by applying the fully explicit method with a known value  $\phi^n$ , that is,

$$\begin{aligned} \frac{\phi_{ij}^{n+1/3} - \phi_{ij}^n}{\Delta t} &= \lambda g_{ij}^2 \phi_{ij}^n \frac{1}{\varepsilon} \sin^2(\pi \phi_{ij}^n), \\ \frac{\phi_{ij}^{n+2/3} - \phi_{ij}^{n+1/3}}{\Delta t} &= -\frac{\pi}{\varepsilon} g_{ij} \sin(2\pi \phi_{ij}^{n+1/3}), \\ \frac{\phi_{ij}^{n+1} - \phi_{ij}^{n+2/3}}{\Delta t} &= 2\varepsilon g_{ij} \Delta_h \phi_{ij}^{n+2/3}. \end{aligned} \quad (30)$$

Also, the edge function  $g(f_0)$  with  $k = 2$  can be numerically computed by

TABLE 3: Elapsed times taken by the proposed method and the reference method [27].

Cases	Proposed method ( $\Delta t$ )	Proposed method ( $\Delta t_{\text{ref}}$ )	Reference ( $\Delta t_{\text{ref}}$ )
$K = 3$	0.315 s	2.297 s	2.843 s
$K = 4$	0.403 s	2.896 s	3.062 s

FIGURE 25: Snapshots of contours are shown in (a), (b), and (c) at  $t = 0$ ,  $t = 2000\Delta t$ , and  $t = 10000\Delta t$ , respectively. Mesh plot of (c) is shown in (d).

$$g(f_0)_{ij} = \frac{1}{1 + (G_\sigma * f_0)_{x,ij}^2 + (G_\sigma * f_0)_{y,ij}^2}, \quad (31)$$

where  $(G_\sigma * f_0)_{x,ij} = [(G_\sigma * f_0)_{i+1,j} - (G_\sigma * f_0)_{i-1,j}]/(2h)$  and  $(G_\sigma * f_0)_{y,ij} = [(G_\sigma * f_0)_{i,j+1} - (G_\sigma * f_0)_{i,j-1}]/(2h)$ . Here,  $(G_\sigma * f_0)_{ij}$  can be computed using a  $3 \times 3$  smoothing kernel as

$$(G_\sigma * f_0)_{ij} = \sum_{m=i-1}^{i+1} \sum_{n=j-1}^{j+1} \frac{f_{0,mm}}{2\pi\sigma^2} e^{-[(i-m)^2 + (j-n)^2]h^2/2\sigma^2}. \quad (32)$$

As mentioned above, the homogeneous Neumann boundary condition is applied to the domain.

**4.1. Synthetic Image 2.** We apply our proposed method to a synthetic image. The synthetic image consists of three rectangles and one circle. That is, we try to separate into four

phases. The initial contour is set to the median of two consecutive numbers of 0, 1, 2, 3, and 4. The size of the image is  $256 \times 256$ . The parameters are chosen as  $\varepsilon = \varepsilon(3h)$ ,  $\Delta t = 5 \text{ e-}6$ ,  $T = 10000\Delta t$ , and  $\lambda = 1 \text{ e}2$ . The results of the synthetic image segmentation can be seen in Figure 25. Figure 25(a) shows the initial contour-shaped rectangular. While Figure 25(b) shows the result at  $t = 2000\Delta t$ , Figure 25(c) shows the result at final time,  $T = 10000\Delta t$ . Figure 25(d) shows the result of multiphase image segmentation in a mesh plot.

**4.2. Segmentation with Real-World Images.** In this section, we applied the proposed method on the real-world images, which are chosen from the CMU-Cornell iCoseg Dataset [46], to demonstrate the robustness of the segmentation. Figure 26 shows the comparison results. Figure 26(a) shows the real-world images of CMU-Cornell iCoseg Dataset. Figure 26(b) shows the results of the proposed method. Figure 26(c) shows the ground truth of the color images. As can

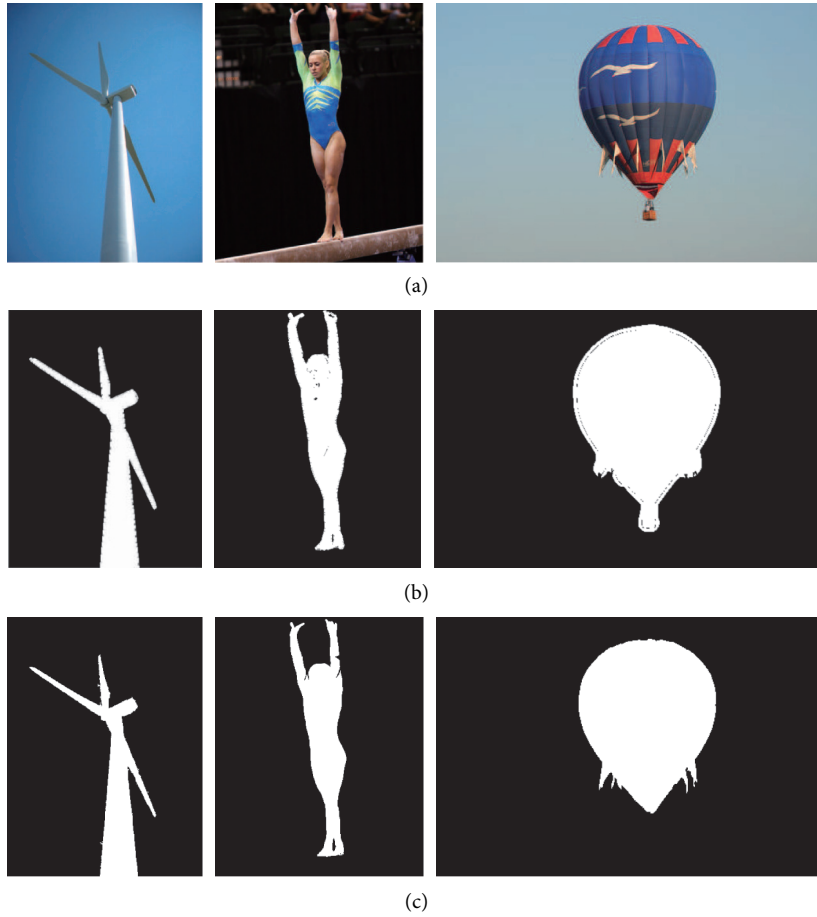


FIGURE 26: Segmentation with the real-world images chosen from the CMU-Cornell iCoseg Dataset: (a) color images, (b) results of the proposed method, and (c) ground truth of the color images.

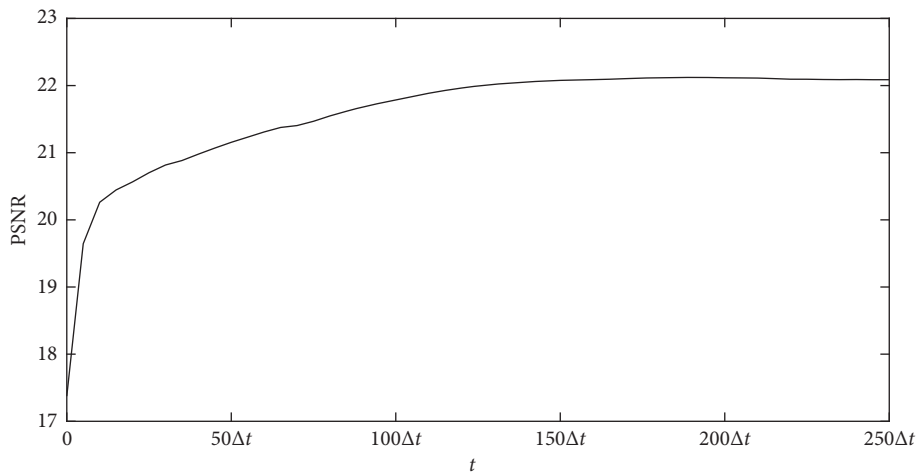


FIGURE 27: Time evolution of a quantitative measure of the segmentation of the proposed method.

be seen from the results, the proposed method can preserve the original shape of the object and shows good performance in image segmentation. Comparing ground truth of the images, we can clearly see that details have been preserved by the proposed method.

4.3. *Measurement of Quality of the Segmentation.* As quantitative measures of the ability to restore damaged fingerprints to the proposed algorithm, we use peak signal-to-noise ratio (PSNR) and structural similarity index map (SSIM), which are defined as follows:

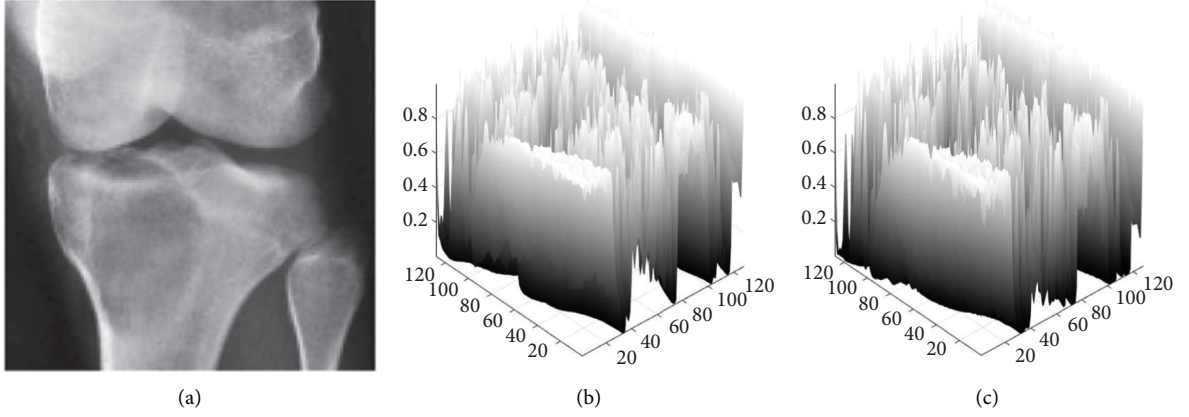


FIGURE 28: (a) Original image. (b) Edge-stopping function  $g$ . (c) Edge-stopping function  $g^2$ .

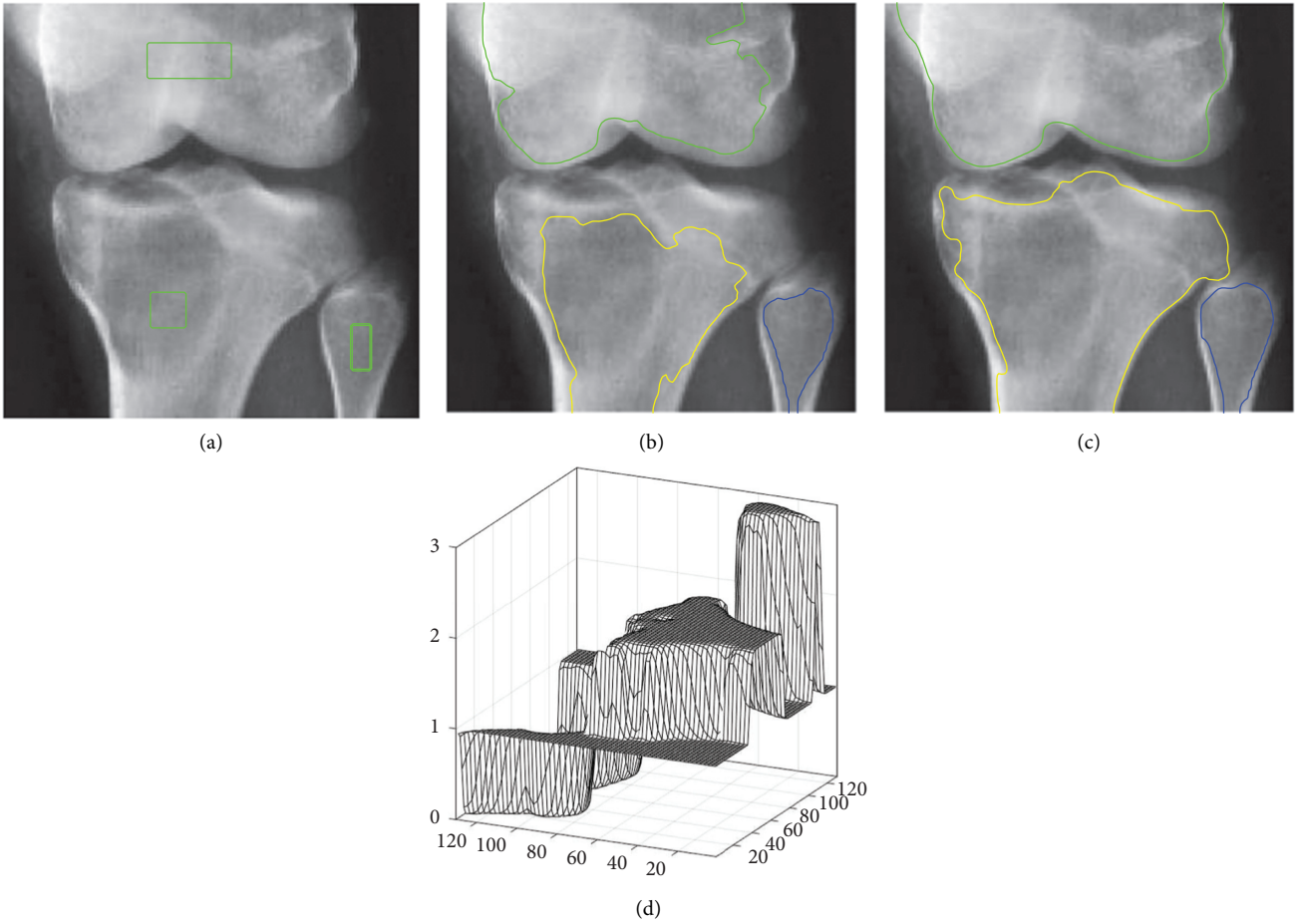


FIGURE 29: Snapshots of contours at (a)  $t = 0$ , (b)  $t = 500000\Delta t$ , and (c)  $t = 1400000\Delta t$ . Mesh plot of (c) is shown in (d).

$$\text{PSNR} = 10 \log_{10} \frac{I_{\max}^2}{\sum_{i=1}^{N_x} \sum_{j=1}^{N_y} (I_{ij} - K_{ij})^2 / (N_x N_y)}, \quad (33)$$

$$\text{SSIM} = \frac{(2\mu_I \mu_K + c_1)(2\sigma_{IK} + c_2)}{(\mu_I^2 + \mu_K^2 + c_1)(\sigma_I^2 + \sigma_K^2 + c_2)},$$

where  $I_{ij} = f_{ij}/(f_{\max} - f_{\min})$ ,  $K_{ij} = 0.5(\phi_{ij} + 1)$ ;  $\mu_I, \mu_K$  denote the average of  $I$  and  $K$ , respectively; and  $\sigma_I^2, \sigma_K^2$  are the variances of  $I$  and  $K$ , respectively. Here,  $\sigma_{IK}$  is the covariance of  $I$  and  $K$ ,  $c_1 = (0.01L)^2$ , and  $c_2 = (0.03L)^2$  with  $L = 1$ . High PSNR and SSIM values indicate a good segmentation of the images.

To verify the efficiency of the proposed method, we compute the average PSNR of the proposed method with the CMU-Cornell iCoseg Dataset, which is shown in Figure 27. From the result, we can see that the curve is increasing, which indicates that the proposed method works well for the image segmentation.

**4.4. X-Ray Example.** We perform the multiphase image segmentation using a knee X-ray as the original image. The size of given image is  $128 \times 128$ . The original image and scalar fields of function  $g$  and  $g^2$  are given in Figure 28. Figure 29 shows the result of multiphase image segmentation in two ways: contour and mesh plot. Here, we use  $\varepsilon = \varepsilon(6h)$  for the width of interfacial region,  $\Delta t = 1 \text{ e-}7$ ,  $T = 1400000\Delta t$ , and  $\lambda = 1 \text{ e}2$ . Initial contours are set to medians between each assigned discrete value of 0, 1, 2, and 3 so that we can get each initialized value (hence only one) between each two successive integers, respectively.

The results yield that the edge-stopping functions  $g$  and  $g^2$  work well and one can easily extract each activated contour only using multiple-well potential.

## 5. Conclusion

In this paper, we present a simple numerical solution algorithm for the gradient flow for the Modica–Mortola functional and numerically investigate its dynamics. We figure out the property of the corresponding gradient flow equation and analyze the effect of parameters. Especially, we analyze the stability of scheme for time step size to our method and examine the goodness of fit of linear relationship for various  $\varepsilon$  values. The results indicate that proper phase separations are achieved via our simple explicit method. The proposed numerical algorithm can be applied to multiphase image segmentation problems. We performed various numerical experiments with synthetic and actual MRI images to show the characteristics of our proposed method. We compared the proposed method to several other existing methods and confirmed that the segmented results are not quite different from those of existing methods. In particular, the implicit method using the multigrid method has a mesh size restriction in common, which is of a multiple of 2; however, our method has the advantage of being free to the mesh size. In addition, our proposed method produces good results in less time even though it has a limitation of time step size. Our method can segment objects of simple color images as shown in Section 4.2. However, it is difficult to achieve good results when segmenting complex color images. Therefore, for future work, we plan to extend the current model to applications, such as complex nature image segmentation [47, 48] and video co-segmentation [49].

## Data Availability

The data used to support the findings of this study are available from the corresponding author upon request.

## Conflicts of Interest

The authors declare that there are no conflicts of interest regarding the publication of this paper.

## Acknowledgments

Yibao Li was supported by the National Natural Science Foundation of China (nos. 11601416 and 11631012). Junseok Kim was supported by the National Research Foundation (NRF), Korea, under project no. BK21 FOUR.

## References

- [1] Y. M. Jung, S. H. Kang, and J. Shen, "Multiphase image segmentation via modica-mortola phase transition," *SIAM Journal on Applied Mathematics*, vol. 67, no. 5, pp. 1213–1232, 2007.
- [2] L. Modica and S. Mortola, "Un esempio di  $\Gamma$ -convergenza," *Bollettino dell'Unione Matematica Italiana B*, vol. 14, pp. 285–299, 1977.
- [3] R. Chen, X. Yang, and H. Zhang, "Decoupled, energy stable scheme for hydrodynamic allen-Cahn phase field moving contact line model," *Journal of Computational Mathematics*, vol. 36, no. 5, pp. 661–681, 2018.
- [4] J. Chen, Z. He, S. Sun, S. Guo, and Z. Chen, "Efficient linear schemes with unconditional energy stability for the phase field model of solid-state dewetting problems," *Journal of Computational Mathematics*, vol. 38, pp. 452–468, 2020.
- [5] B. Bogosel, D. Bucur, and I. Fragalà, "Phase field approach to optimal packing problems and related Cheeger clusters," *Applied Mathematics and Optimization*, vol. 81, no. 1, pp. 63–87, 2020.
- [6] E. Oudet and F. Santambrogio, "A modica-mortola approximation for branched transport and applications," *Archive for Rational Mechanics and Analysis*, vol. 201, no. 1, pp. 115–142, 2011.
- [7] S. Conti, M. Rumpf, R. Schultz, and S. Tölkes, "Stochastic dominance constraints in elastic shape optimization," *SIAM Journal on Control and Optimization*, vol. 56, no. 4, pp. 3021–3034, 2018.
- [8] P. Pegon, F. Santambrogio, and Q. Xia, "A fractal shape optimization problem in branched transport," *Journal de Mathématiques Pures et Appliquées*, vol. 123, pp. 244–269, 2019.
- [9] S. Ha Kang, B. Sandberg, B. Sandberg, and M. Yip, "A regularized k-means and multiphase scale segmentation," *Inverse Problems and Imaging*, vol. 5, no. 2, pp. 407–429, 2011.
- [10] M. Wang, C. Huang, C. Zeng, and C. H. Lai, "Two-phase image inpainting: combine edge-fitting with PDE inpainting," *Advances in Applied Mathematics and Mechanics*, vol. 4, no. 6, pp. 769–779, 2012.
- [11] T. Barbu and C. Moroşanu, "Image restoration using a nonlinear second-order parabolic PDE-based scheme," *Analele Universitatii "Ovidius" Constanta - Seria Matematica*, vol. 25, no. 1, pp. 33–48, 2017.
- [12] T. Barbu, "Second-order anisotropic diffusion-based framework for structural inpainting," *Proceedings of the Romanian Academy A*, vol. 19, pp. 329–336, 2018.
- [13] J. Dobrosotskaya and W. Guo, "A PDE-free variational method for multi-phase image segmentation based on multiscale sparse representations," *Journal of Imaging*, vol. 3, no. 3, p. 26, 2017.

- [14] Y. Liu, C. He, Y. Wu, and Z. Ren, "The  $L_0$ -regularized discrete variational level set method for image segmentation," *Image and Vision Computing*, vol. 75, pp. 32–43, 2018.
- [15] G. Huang, H. Ji, and W. Zhang, "A fast level set method for inhomogeneous image segmentation with adaptive scale parameter," *Magnetic Resonance Imaging*, vol. 52, pp. 33–45, 2018.
- [16] Y. Li, "Image segmentation via image decomposition and fuzzy region competition," *Journal of Visual Communication and Image Representation*, vol. 30, pp. 328–342, 2015.
- [17] L. S. Cigaroudy and N. Aghazadeh, "A multiphase segmentation method based on binary segmentation method for Gaussian noisy image," *Signal, Image and Video Processing*, vol. 11, no. 5, pp. 825–831, 2017.
- [18] Y. Hu, Y. Li, R. Song, P. Rao, and Y. Wang, "Minimum barrier superpixel segmentation," *Image and Vision Computing*, vol. 70, pp. 1–10, 2018.
- [19] J. Liu, X.-c. Tai, S. Leung, and H. Huang, "A new continuous max-flow algorithm for multiphase image segmentation using super-level set functions," *Journal of Visual Communication and Image Representation*, vol. 25, no. 6, pp. 1472–1488, 2014.
- [20] A. Badoual, M. Unser, and A. Depeursinge, "Texture-driven parametric snakes for semi-automatic image segmentation," *Computer Vision and Image Understanding*, vol. 188, Article ID 102793, 2019.
- [21] M. U. Rehman, D. Baleanu, J. Alzabut, M. Ismail, and U. Saeed, "Greenhaar wavelets method for generalized fractional differential equations," *Advances in Difference Equations*, vol. 2020, no. 1, pp. 1–25, 2020.
- [22] B. Ghanbari and A. Atangana, "Some new edge detecting techniques based on fractional derivatives with non-local and non-singular kernels," *Advances in Difference Equations*, vol. 2020, no. 1, pp. 1–19, 2020.
- [23] W. Zhang, L. Jin, E. Song, and X. Xu, "Removal of impulse noise in color images based on convolutional neural network," *Applied Soft Computing*, vol. 82, Article ID 105558, 2019.
- [24] L. S. Tan, Z. Zainuddin, and P. Ong, "Wavelet neural networks based solutions for elliptic partial differential equations with improved butterfly optimization algorithm training," *Applied Soft Computing*, vol. 95, Article ID 106518, 2020.
- [25] F. Isensee, P. F. Jaeger, S. A. A. Kohl, J. Petersen, and K. H. Maier-Hein, "nnU-Net: a self-configuring method for deep learning-based biomedical image segmentation," *Nature Methods*, vol. 18, no. 2, pp. 203–211, 2021.
- [26] J. Ma, J. Chen, M. Ng et al., "Loss odyssey in medical image segmentation," *Medical Image Analysis*, vol. 71, Article ID 102035, 2021.
- [27] Y. Li and J. Kim, "Multiphase image segmentation using a phase-field model," *Computers & Mathematics with Applications*, vol. 62, no. 2, pp. 737–745, 2011.
- [28] F.-R. Lin and S.-W. Yang, "A two-stage method for piecewise-constant solution for Fredholm integral equations of the first kind," *Mathematics*, vol. 5, no. 2, p. 28, 2017.
- [29] M. Huska, A. Lanza, S. Morigi, and F. Sgallari, "Convex non-convex segmentation of scalar fields over arbitrary triangulated surfaces," *Journal of Computational and Applied Mathematics*, vol. 349, pp. 438–451, 2019.
- [30] H. G. Lee and J.-Y. Lee, "A second order operator splitting method for Allen-Cahn type equations with nonlinear source terms," *Physica A: Statistical Mechanics and Its Applications*, vol. 432, pp. 24–34, 2015.
- [31] L. N. Guin and H. Baek, "Comparative analysis between prey-dependent and ratio-dependent predator-prey systems relating to patterning phenomenon," *Mathematics and Computers in Simulation*, vol. 146, pp. 100–117, 2018.
- [32] Y. Li and J. Kim, "An unconditionally stable numerical method for bimodal image segmentation," *Applied Mathematics and Computation*, vol. 219, no. 6, pp. 3083–3090, 2012.
- [33] S. Zhu and R. Gao, "A novel generalized gradient vector flow snake model using minimal surface and component-normalized method for medical image segmentation," *Biomedical Signal Processing and Control*, vol. 26, pp. 1–10, 2016.
- [34] F. V. Farahani, A. Ahmadi, and M. H. F. Zarandi, "Hybrid intelligent approach for diagnosis of the lung nodule from CT images using spatial kernelized fuzzy c-means and ensemble learning," *Mathematics and Computers in Simulation*, vol. 149, pp. 48–68, 2018.
- [35] H. Shah, N. Badshah, F. Ullah, and A. Ullah, "A new selective segmentation model for texture images and applications to medical images," *Biomedical Signal Processing and Control*, vol. 48, pp. 234–247, 2019.
- [36] E. E. Nithila and S. S. Kumar, "Segmentation of lung from CT using various active contour models," *Biomedical Signal Processing and Control*, vol. 47, pp. 57–62, 2019.
- [37] N. Badshah, H. Rabbani, and H. Atta, "On local active contour model for automatic detection of tumor in MRI and mammogram images," *Biomedical Signal Processing and Control*, vol. 60, Article ID 101993, 2020.
- [38] B. Han and Y. Wu, "Active contours driven by global and local weighted signed pressure force for image segmentation," *Pattern Recognition*, vol. 88, pp. 715–728, 2019.
- [39] C. Liu, M. K.-P. Ng, and T. Zeng, "Weighted variational model for selective image segmentation with application to medical images," *Pattern Recognition*, vol. 76, pp. 367–379, 2018.
- [40] F. Li, S. Osher, J. Qin, and M. Yan, "A multiphase image segmentation based on fuzzy membership functions and  $L_1$ -norm fidelity," *Journal of Scientific Computing*, vol. 69, no. 1, pp. 82–106, 2016.
- [41] S. Esedoglu and R. March, "Segmentation with depth but without detecting junctions," *Journal of Mathematical Imaging and Vision*, vol. 18, no. 1, pp. 7–15, 2003.
- [42] P. Yue, C. Zhou, and J. J. Feng, "Sharp-interface limit of the Cahn-Hilliard model for moving contact lines," *Journal of Fluid Mechanics*, vol. 645, pp. 279–294, 2010.
- [43] L. A. van der Kleij, J. de Bresser, J. Hendrikse, J. C. W. Siero, E. T. Petersen, and J. B. De Vis, "Fast CSF MRI for brain segmentation; Cross-validation by comparison with 3D T1-based brain segmentation methods," *PLoS One*, vol. 13, no. 4, Article ID e0196119, 2018.
- [44] G. A. Ladinsky, B. Vasilic, A. M. Popescu et al., "Trabecular structure quantified with the MRI-based virtual bone biopsy in postmenopausal women contributes to vertebral deformity burden independent of areal vertebral BMD," *Journal of Bone and Mineral Research: The Official Journal of the American Society for Bone and Mineral Research*, vol. 23, no. 1, pp. 64–74, 2008.
- [45] S. H. Kang and R. March, "Multiphase image segmentation via equally distanced multiple well potential," *Journal of Visual Communication and Image Representation*, vol. 25, no. 6, pp. 1446–1459, 2014.
- [46] D. Batra, A. Kowdle, D. Parikh, J. Luo, and T. Chen, "iCoseg: interactive co-segmentation with intelligent scribble guidance," in *Proceedings of the 2010 IEEE Computer Society Conference on Computer Vision and Pattern Recognition*, pp. 3169–3176, San Francisco, CA, USA, June 2010.
- [47] X. Dong, J. Shen, L. Shao, and L. Van Gool, "Sub-Markov random walk for image segmentation," *IEEE Transactions on Image Processing*, vol. 25, no. 2, pp. 516–527, 2015.

- [48] J. Shen, X. Dong, J. Peng, X. Jin, L. Shao, and F. Porikli, "Submodular function optimization for motion clustering and image segmentation," *IEEE Transactions on Neural Networks and Learning Systems*, vol. 30, no. 9, pp. 2637–2649, 2019.
- [49] W. Wenguan Wang, J. Jianbing Shen, X. Xuelong Li, and F. Porikli, "Robust video object cosegmentation," *IEEE Transactions on Image Processing*, vol. 24, no. 10, pp. 3137–3148, 2015.